Evidence for early life in Earth's oldest hydrothermal vent precipitates

M.S. Dodd[a,b], D. Papineau[a,b], T. Grenne[c], J.F. Slack[d], M. Rittner[b], F. Pirajno[e] J. O'Neil[f], C.T.S. Little[g]

[a]London Centre for Nanotechnology, 17-19 Gordon Street, London WC1H 0AH UK
[b]Department of Earth Sciences, University College London, Gower Street, London WC1E 6BT UK
[c]Geological Survey of Norway, Leiv Eirikssons vei 39, 7491 Trondheim Norway
[d]U.S. Geological Survey, National Center, MS 954, Reston, VA 20192 USA
[e]Centre for Exploration Targeting, The University of Western Australia, 35 Stirling Highway, Crawley, WA 6009 Australia
[f]Department of Earth and Environmental Sciences, University of Ottawa, Ottawa, K1N 6N5 Canada
[g]School of Earth and Environment, University of Leeds, Leeds LS2 9JT UK

Although it is not known when or where life on Earth began, some of the earliest habitable environments may have been submarine-hydrothermal vents. Here we report putative fossilised microorganisms at least 3770 and possibly 4290 million years old in ferruginous sedimentary rocks, interpreted as seafloor-hydrothermal vent-related precipitates, from the Nuvvuagittuq belt in Canada. These structures occur as micron-scale haematite tubes and filaments with morphologies and mineral assemblages similar to filamentous microbes from modern hydrothermal vent precipitates and analogous microfossils in younger rocks. The Nuvvuagittuq rocks contain isotopically light carbon in carbonate and carbonaceous material, which occurs as graphitic inclusions in diagenetic carbonate rosettes, apatite blades intergrown among carbonate rosettes, magnetite-haematite granules, and associated with carbonate in direct contact with the putative microfossils. Collectively, these observations are consistent with an oxidised biomass and provide evidence for biological activity in submarine-hydrothermal environments more than 3770 million years ago.

There are no confirmed microfossils older than 3500 million years (Myr) on Earth, probably because of the highly metamorphosed nature of the oldest sedimentary rocks[1]. Therefore, studies to date have focused almost exclusively on chemical traces and primarily on the isotopic composition of carbonaceous material (CM), which has led to controversies on the origin of isotopically light reduced carbon[2]. Schists from the ca.

3700 Myr old Isua Supracrustal Belt, southwest Greenland, contain up to 8.8 wt% graphitic carbon depleted in ^{13}C attributed to biological activity[3,4]. However, because non-biological decarbonation reactions and Fischer-Tropsch-type synthesis[5] are capable of producing reduced carbon with similar isotopic compositions, non-biological interpretations are possible[2]. Apatite with graphite coatings, within iron formations (IF) from the ca. 3830 Myr old Akilia supracrustal belt, southwest Greenland, has been interpreted as the metamorphosed product of biogenic matter[6], supported by the presence of biologically important heteroatoms within the graphite[7,8]. However, it has been suggested that some graphite in the Akilia IF was deposited by metamorphic fluids [8,9]. This latter interpretation is echoed in the Nuvvuagittuq supracrustal belt (NSB) by the presence of poorly crystalline, fluid-deposited graphite that coats apatite[10], demonstrating that some apatite-graphite occurrences are produced abiotically during fluid remobilization and high-grade metamorphism.

The NSB in northeastern Canada represents a fragment of Earth's primitive mafic oceanic crust. The NSB is composed predominantly of basaltic metavolcanic rocks (Fig. E1), which locally preserve pillow lava structures[11] consistent with a submarine setting, and of chemical sedimentary units including IFs and minor jasper (quartz-rich rocks with haematite and magnetite) and carbonate-bearing IF. The IF units occur between sequences of tholeiitic and calc-alkaline metabasalts, suggesting deposition at the same stage of volcanic evolution and seafloor-hydrothermal activity. The minimum age for the belt is constrained by cross-cutting trondhjemitic intrusive rocks that yield U-Pb zircon ages of 3774 to 3751 Myr[12,13]. Furthermore, ^{146}Sm-^{142}Nd systematics suggest an age of 4290 Myr for the metabasaltic unit of the NSB[14,15]. The exact age of the NSB is debated (see Supplementary Information); nonetheless, the NSB includes one of the oldest—if not the oldest—IFs known on Earth. The IF has seawater-like chemical signatures[16,17] and heavy Fe isotopic compositions[17,18], consistent with formation by precipitation of iron derived from hydrothermal fluids associated with volcanism[19]. Bulk-rock rare earth element data for the NSB jasper and carbonate IF—especially the presence of positive Eu anomalies—suggest a link to sea-floor hydrothermal activity (Fig. E2). The presence of well-preserved, 20-3000 μm sized chalcopyrite crystals within the NSB jasper and carbonate IF (Fig. E3A) demonstrate the lack of post-depositional oxidation.

Most NSB rocks were subjected to upper amphibolite-facies metamorphism ca. 2700 Myr ago[14,20]. Here we describe parts of the NSB that were less affected by deformation (Table S4) and focus on sites where metamorphism appears not to exceed lower amphibolite facies[17]. This setting is evidenced by local outcrops in the southwestern margins of the belt that preserve primary chert, diagenetic calcite rhombohedra with poikilitic textures, and minerals of low metamorphic grade such as euhedral stilpnomelane and minnesotaite in chert that lack pseudomorphic retrograde textures.

Haematite tubes and filaments

Modern hydrothermal Si-Fe deposits host communities of microorganisms, some of which are Fe-oxidising bacteria that form distinctive tubes and filaments [21-26]. Epifluorescence imaging of modern vent samples has shown that cylindrical casts composed of Fe-oxyhydroxide are formed by bacterial cells and are undeniably biogenic[25]. Hence, morphologically similar tubes and filaments in ancient jaspers may be taken as biosignatures[25,27-30] that can survive elevated temperatures and pressures[31], even though such jaspers generally lack CM[22,28,32,33]. The presence of abundant microcrystalline quartz in jaspers may provide strong protection of primary features, such that deformation and metamorphism do not obliterate all depositional and diagenetic textures preserved by haematite[29].

Haematite filaments in the NSB jasper are between 2 and 14 μm in diameter and up to 500 μm in length (Fig. 1; E4). Some of the filaments exhibit loose coiling (Fig. E4A), some are branched (Fig. 1C), and some form twisting plates of haematite around a core that radiate from terminal knobs (Fig. E4C). They occur within quartz layers of the jaspers, in mm-size domains together with haematite rosettes (Fig. 1C) and comprise micron-size grains of haematite that are in turn enveloped by nanoscale haematite (Fig. 1D). Cross-polar images show that the filaments do not occur along grain boundaries (Fig. 1D). Some filaments are associated with micron-sized carbonate grains, which locally occur together with graphite (Fig. E5). The NSB filaments (Fig. 1A-D) have morphologies and compositions similar to filaments that occur commonly in Phanerozoic jaspers of seafloor-hydrothermal origin, such as those from Løkken, Norway (see Supplementary Information;) ca. 480 Myr; (Fig. 1B) and the Franciscan Complex, California (ca. 185 Myr)[33]. The NSB filaments are also similar to microbial filaments found in modern low-temperature

hydrothermal vents [23,26], some of which display twisted and branched morphologies known to be formed by iron-oxidising bacteria[21,26,30].

Within the NSB jasper, cylindrical tubes having walls composed of dense nanoscale haematite grains are preserved within coarse (50-500 μm) quartz, which encapsulates the entire structure and fills the centres (Fig. 2). Depth reconstructions demonstrate the consistent shape of the tubes and filaments along their lengths and the cylindrical morphology of the tubes in 3D (Fig. 2B, E4). The tubes are straight, have diameters of 16-30 μm (Fig. E4), and vary in length from 80 to 400 μm. Most tubes are filled with quartz only, but some encapsulate a filament composed of micron-sized, platy grains of haematite that extend radially outward from the core of the filament (Fig. 2C), similar to those in younger jaspers (Fig. 2G). The NSB tubes form aligned clusters within patches of locally coarser quartz (Fig. 2A, E), similar to tubes in the Løkken jaspers (Fig. 2H), and occur in lamination-deflecting, concretionary structures (Fig. E3B-C) and within quartz layers between mm-thick haematite-magnetite layers (Fig. E3F). About one in ten tubes in the NSB terminate with a haematite knob (80-120 μm in diameter); about half of those have a second tube attached (Fig. 1A; 2F).

The tubes exhibit features attributed in other seafloor-hydrothermal jaspers to fossil remains of iron-oxidising bacteria[28]: (1) tubes contain internal haematite filaments, similar to those of modern microbial remains[23,26]; (2) some tubes are attached to terminal haematite knobs, like microbial tubes documented throughout the geological record[28,32] and in modern hydrothermal precipitates[21,24]; (3) uniform tube diameters are in the same 16-30 μm range as that of tube microfossils in the Mt. Windsor and Uralian jaspers[29,34]; (4) tubes are aligned in a similar direction (as in some ancient jaspers[34]), which is characteristic of some modern iron-oxidising bacteria[24,28,30,35]; and (5) tubes and filaments co-occur with apatite, carbonate, and CM as in microfossils within the Løkken (Fig. E5) and other Phanerozoic jaspers[36].

To assess the biogenicity of the NSB putative microfossils we consider as a null hypothesis plausible abiogenic mechanisms that could create haematite tubes and filaments through metamorphic stretching or diagenetic processes (see Supplementary Information), such as fluid flow, precipitation reactions and self-assembly. However, no known mechanism can wholly facilitate the growth of multiple tubes from a single haematite knob at varying angles (Fig. 1A, E4) during metamorphic or diagenetic reactions, together with

the formation of internal coiled, branched, and twisted filaments (Fig. E4) with haematite envelopes (Fig. 1C), in addition to their close spatial association with carbonate and graphitic carbon (Fig. E5). Collectively, our observations cannot be explained by a single or combined abiogenic pathway, thus we reject the null hypothesis.

Uniformitarianism, epitomised by younger examples of microbially-produced haematite tubes in hydrothermal vent precipitates throughout the geological record (Table S5), leads us to conclude that haematite tubes and filaments within the NSB jaspers are mineralised remains of bacterial sheaths and extracellular filaments. Filaments were likely coated by Fe-oxyhydroxide or silica after being discarded by the microbes, and subsequently coated with silica and recoated by Fe-oxyhydroxide in successive venting cycles[23,35], producing thicker filament structures than the initial structure. Residual CM from the microbes is now preserved in association with carbonate in contact with the filaments. Whereas tubes and filaments in younger jaspers are typically attributed to Fe-oxidisers, other bacteria such as cyanobacteria may produce aligned[37], hollow cylindrical casts of iron oxide[38]. However, the attachment of filaments to terminal knobs is characteristic of some iron-oxidisers in hydrothermal systems[21], but not of cyanobacteria. These knobs are morphologically similar to bacterial cells of the anoxygenic-photoferrotroph *Hyphomicrobium*, which produces stalks during reproduction. Alternatively, the knobs may be better compared to bacterial holdfasts created by chemolithotroph *Leptothrix*-type bacteria. A twisted morphology in some filaments also closely resembles the iron-rich stalks formed by the extant ζ-proteobacterium *Mariprofundus*.

Carbonate rosettes, apatite, and carbonaceous material

If biological processes were involved in IF genesis, the characteristic absence of CM in IFs may be due to organisms such as photoferrotrophs that separate ferric iron from the cells and allow most CM to escape sedimentation[39]. Any CM that enters the sediments may be diagenetically oxidised in conjunction with the reduction of ferric iron[40]. This reaction may be understood from the following equation

$$CH_3COOH + 8Fe(OH)_3 + 2H_2O \rightarrow 8Fe^{2+} + 2HCO_3^- + 22OH^- + 8H^+$$

A consequence of these reactions is the oxidation of CM to carbonate and the reduction insoluble ferric iron into soluble ferrous iron, followed by precipitation as iron-bearing carbonate, ferrous silicates and

magnetite. The formation of carbonate from oxidised CM is well-illustrated in the ca. 2470 Myr Brockman IF of Western Australia (Fig. E6H-I), where carbonate rhombohedra enclose layers of disseminated CM, mixed with carbonate rosettes.

Particularly significant is the presence of carbonate rosettes, 50-200 μm in diameter, that typically contain microscopic inclusions of CM. Such rosettes are found in the NSB IFs (Fig. 3; E6) as well as in younger jaspers and IFs (Table S6). In the Løkken jasper, for example, carbonate rosettes with CM inclusions overgrow haematite filaments (Fig. E6K) attributed to mineralised bacteria[27]. In this interpretation, CM was sourced from the bacteria. Carbonate rosettes have also been grown in diagenetic experiments using ferrihydrite and CM[40].

Both NSB and ancient jaspers, and modern hydrothermal vent precipitates, commonly preserve haematite rosettes[27,32,41] (Table S7) (Fig. E7) albeit of debated origin[42]. Ferrihydrite rosettes that form today in the Lau Basin are intimately associated with microbial filaments, but may be a result of abiogenic precipitation[41]. In the Løkken jaspers, haematite rosettes are attributed to Fe-Si gel maturation on the seafloor[27]. Such textural relationships may require micro-chemical Eh-pH gradients that reduce ferric iron, followed by mobilisation and oxidation of Fe^{2+} and re-precipitation as haematite. Given their close proximity to microbial filaments today[41], it is plausible microbial CM served as a reductant.

Sub-spheroidal rosettes of Fe-calcite (Table S8) in carbonate-rich IFs from the NSB (Fig. 3; E6A-B) have quartz cores and dimensions of ca. 50 to 200 μm[19]. Some carbonate rosettes locally contain apatite inclusions and are cut by apatite laths hundreds of microns in length (Fig. 3G), and by acicular stilpnomelane that cuts both rosettes and apatite (Fig. 3; E6G), demonstrating that the apatite and rosettes are pre-metamorphic. The apatite contains myriad inclusions of aqueous fluid, haematite, magnetite, and CM (Fig. 3F-H). Moreover, the rosettes occur with micron-size particles of graphitic carbon, randomly disseminated throughout the rings and surrounding chert (Fig. 3C). Raman spectra of the graphitic carbon show sharp and prominent G-bands ranging from 1565 to 1584 cm^{-1} and minor D-bands from 1331 to 1349 cm^{-1} (Fig. 3J; E6E). While apatite-hosted CM displays Raman G-peak positions consistent with graphitic carbon, the broad D-band suggests the presence of disordered sp3-bonded carbon (Fig. 4J) or a contribution from nanoscale haematite, which has a broad peak at 1320 cm^{-1}, partly explaining the broad and intense

Raman D-peak. Fe-oxides can be seen associated with CM in transmitted light and by micro-Raman (Fig. E8D). Raman spectra of graphitic carbon within the carbonate rosettes (Fig. 3J) yield a range of calculated crystallisation temperatures between 396 and 564°C (Table S9-10)[43], which is partly consistent with mineral geothermometers obtained from the Ujaraaluk amphibolite[17], distinct from poorly crystalline, fluid-deposited graphite in silicate BIF from other parts of the NSB[10] (Fig. E8; Table S11). Additionally, Raman spectra of graphitic carbon found in layered jaspers of the NSB (Fig. E8B-E) show that graphite from two different samples shares common crystallisation temperatures of ca. 500°C. The formation of syngenetic carbon preserved as graphite can be explained by the production of CM via abiogenic synthesis[5], carbonate decarbonation[2], or from an original microbial biomass.

Isotopically light carbonate (–15 to –5‰) in IFs has been attributed to the oxidation of isotopically light CM derived from microbial activity[44], but precludes neither the oxidation of isotopically light abiogenic CM, nor a contribution from marine carbonate. The $\delta^{13}C_{carb}$ and $\delta^{13}C_{org}$ values for jaspers from the NSB are –8.3 to –6.7‰ and –25.7 to –19.7‰, respectively[10], consistent with a biogenic origin, although not unambiguously. However in the case of the NSB, the phosphorus (an element vital in biology) in laths of apatite intergrown with the graphite-bearing carbonate rosettes suggests a biological source for the carbon in graphite. In modern ocean sediments, accumulations of CM on the seafloor may concentrate phosphorus through biological metabolisms[45]. Furthermore, the presence of apatite in some NSB carbonate rosettes is analogous to apatite rosettes between stromatolitic phosphorite columns in flourishing late Palaeoproterozoic microbial ecosystem[46]. Whereas structures similar to carbonate rosettes may form in open spaces and cavities such as stalactites[47], the well-banded, siliceous-carbonate gels that formed precursors to these carbonate IFs could not have had a porous texture, hence formation of carbonate rosettes by open-space filling can be ruled out. This is reinforced by the presence of morphologically similar, diagenetic graphite-bearing carbonate rosettes in the Løkken jasper[27] (Fig. E6J-M). Combined with evidence of filamentous microfossils and their direct association with carbonate and graphitic carbon, and with numerous other observations supporting biological activity in the NSB, the carbonate rosettes are best explained as having formed by the oxidation of biomass. Such reactions may have proceeded as chemically

oscillating reactions akin to the Belousov-Zhabotinsky reaction[48], in line with inferences from similar structures in younger IFs (Fig. E6H-M) and diagenetic experiments[40].

Granules

Magnetite-rimmed granules are common in late Palaeoproterozoic IFs and typically occur between stromatolite columns (Fig. E3I) and host microfossils. The oldest known granular IF from the Mozaan Group, South Africa, is ca. 2,900 Myr old and contains magnetite-rimmed granules, isotopically light carbonate, and zero to positive δ^{56}Fe values suggesting a role from iron-oxidising microbes[49].

Comparable 100-500 μm spheroidal to sub-spheroidal granules occur in the NSB jaspers that crop out together with the carbonate IF and banded jaspers hosting the microfossils (Fig. E3B, F). These granules occur in a matrix of chert (Fig. 4C) and have rims composed of coarse magnetite with interiors of coarser grained quartz compared to the matrix. Micro-Raman images reveal that the granules contain micron-sized stilpnomelane, magnetite, calcite, haematite, apatite, and CM (Fig. 4D). Inclusions of CM within the granules are 1-4 μm in size and display a predominant Raman peak at ca. 1560-1580 cm^{-1} and a broad poorly-resolved D-peak (Fig. 4E). Granules of a similar size (200-400 μm) in jaspers from the late Palaeoproterozoic Biwabik IF (Fig. 4A) and the Løkken jasper (Fig. E9I) also contain quartz coarser than in the surrounding matrix, and a comparable mineralogy dominated by magnetite-rimmed granules accompanied by haematite, carbonate, CM, and ferrous silicates. CM within granules from all these jaspers is typically associated with, and coats micron-size diagenetic carbonate (Fig. E9). This close spatial association and the occurrence of CM concentrated in diagenetic granules suggest that such CM is a primary phase. Less commonly, Løkken granules contain haematite filaments with terminal knobs (Fig. E9L).

We propose that the mineralogical constituents of iron-oxide granules of these jaspers reflect oxidation-reduction reactions. This model implicates CM and ferric iron as original reactants, whereas ferric-ferrous silicates, apatite, magnetite, and carbonate are considered reaction products. Given the similar morphology, mineralogy, composition, and common occurrence of rosettes, granules, and filamentous microfossils in the Biwabik, Løkken, and NSB jaspers, these diagenetic reactions would have proceeded in a similar manner.

This conclusion and the well-documented occurrence of microfossils within some granules[50] (Fig. E9L) point to an origin involving microorganisms on the Nuvvuagittuq seafloor.

Preservation in the NSB of CM and minerals in diagenetic rosettes and granules that formed from the oxidation of biomass, together with the presence of tubes similar in mineralogy and morphology to those in younger jaspers interpreted as microfossils, reveal that life established a habitat near submarine-hydrothermal vents before 3770, possibly as early as 4290 Myr ago. On the basis of chemical and morphological lines of evidence, the tubes and filaments are best explained as remains of iron-metabolising filamentous bacteria, therefore representing one of the oldest life forms recognized on Earth. Given this new evidence from the NSB, ancient submarine-hydrothermal vent systems should be viewed as potential sites for the origins of life on Earth, and thus primary targets in the search for extraterrestrial life.

Acknowledgements

M.S.D. and D.P. acknowledge support from UCL and the LCN, and a DTG from EPSRC, UK. D.P. also thanks the NASA Astrobiology Institute (Grant No. NNA04CC09A), the Carnegie Institution of Washington and Carnegie of Canada for funding, and the Geological Survey of Western Australia for access and support in the core library. We are grateful to the municipality of Inukjuak, Québec, and the Pituvik Landholding Corporation for permission to work on their territory, and to M. Carroll for logistical support. We thank J. Davy and A. Beard for assistance with sample preparation and SEM and EPMA analyses, and S. Huo for help with FIB nano-fabrication. We also thank G. and Y. Shields-Zhou and P. Pogge Von Strandmann for comments on the manuscript and K. Konhauser for a critical review.

Author Contributions

M.S.D. and D.P. designed the research and performed micro-analyses. They also wrote the manuscript which received important contributions from all co-authors. M.R. conducted LA-ICP-MS analyses. T.G. provided support for field work in Norway. T.G., J.F.S., F.P., and D.P. all supplied samples crucial to the work.

Author Information

Reprints and permissions information is available at www.nature.com/reprints

Correspondence and requests for materials should be addressed to d.papineau@ucl.ac.uk

Competing financial interests

The authors declare no competing financial interests.

Data availability statement

The data that support the findings of this study are available from the corresponding author upon reasonable request.

1 Bernard, S. & Papineau, D. Graphitic Carbons and Biosignatures. *Elements* **10**, 435-440, doi:10.2113/gselements.10.6.435 (2014).

2 Van Zuilen, M. A., Lepland, A. & Arrhenius, G. Reassessing the evidence for the earliest traces of life. *Nature* **418**, 627-630 (2002).

3 Ohtomo, Y., Kakegawa, T., Ishida, A., Nagase, T. & Rosing, M. T. Evidence for biogenic graphite in early Archaean Isua metasedimentary rocks. *Nature Geoscience* **7**, 25-28, doi:10.1038/ngeo2025 (2013).

4 Rosing, M. T. 13C-Depleted Carbon Microparticles in 3700Ma Sea-floor sedimentary rocks from West Greenland. *Science* **283**, 674-676, doi:10.1126/science.283.5402.674 (1999).

5 McCollom, T. M. & Seewald, J. S. Abiotic synthesis of organic compounds in deep-sea hydrothermal environments. *Chemical reviews* **107**, 382-401 (2007).

6 Mojzsis, S. J. *et al.* Evidence for life on Earth before 3,800 million years ago. *Nature* **384**, 55-59 (1996).

7 Papineau, D. *et al.* Ancient graphite in the Eoarchean quartz-pyroxene rocks from Akilia in southern West Greenland II: Isotopic and chemical compositions and comparison with Paleoproterozoic

banded iron formations. *Geochimica Cosmochimica Acta* **74**, 5884-5905, doi:10.1016/j.gca.2010.07.002 (2010).

8 Papineau, D. *et al.* Ancient graphite in the Eoarchean quartz–pyroxene rocks from Akilia in southern West Greenland I: Petrographic and spectroscopic characterization. *Geochimica Cosmochimica Acta* **74**, 5862-5883, doi:10.1016/j.gca.2010.05.025 (2010).

9 Lepland, A., van Zuilen, M. A. & Philippot, P. Fluid-deposited graphite and its geobiological implications in early Archean gneiss from Akilia, Greenland. *Geobiology* **9**, 2-9, doi:10.1111/j.1472-4669.2010.00261.x (2011).

10 Papineau, D. *et al.* Young poorly crystalline graphite in the >3.8-Gyr-old Nuvvuagittuq banded iron formation. *Nature Geoscience* **4**, 376-379, doi:10.1038/ngeo1155 (2011).

11 O'Neil, J., Francis, D. & Carlson, R. W. Implications of the Nuvvuagittuq greenstone belt for the formation of Earth's early crust. *Journal of Petrology* **52**, 985-1009, doi:10.1093/petrology/egr014 (2011).

12 Cates, N. L., Ziegler, K., Schmitt, A. K. & Mojzsis, S. J. Reduced, reused and recycled: Detrital zircons define a maximum age for the Eoarchean (ca. 3750–3780Ma) Nuvvuagittuq Supracrustal Belt, Québec (Canada). *Earth and Planetary Science Letters* **362**, 283-293, doi:10.1016/j.epsl.2012.11.054 (2013).

13 Darling, J. R. *et al.* Eoarchean to Neoarchean evolution of the Nuvvuagittuq Supracrustal belt: New insights from U-Pb zircon geochronology. *Am J Sci* **313**, 844-876, doi:10.2475/09.2013.02 (2013).

14 O'Neil, J., Carlson, R. W., Paquette, J.-L. & Francis, D. Formation age and metamorphic history of the Nuvvuagittuq Greenstone Belt. *Precambrian Research* **220-221**, 23-44, doi:10.1016/j.precamres.2012.07.009 (2012).

15 O'Neil, J., Carlson, R. W., Francis, D. & Stevenson, R. K. Neodymium-142 Evidence for Hadean mafic crust. *Science* **321**, 1828-1831 (2008).

16 Mloszewska, A. M. *et al.* The composition of Earth's oldest iron formations: The Nuvvuagittuq Supracrustal Belt (Québec, Canada). *Earth and Planetary Science Letters* **317-318**, 331-342, doi:10.1016/j.epsl.2011.11.020 (2012).

17 O'Neil, J. *et al.* in *Earth's Oldest Rocks* Vol. 15 (eds Martin J. van Kranendonk, R. Hugh Smithies, & Vickie C. Bennett) 219-250 (Elsevier B.V, 2007).

18 Dauphas, N., Cates, N. L., Mojzsis, S. J. & Busigny, V. Identification of chemical sedimentary protoliths using iron isotopes in the >3750 Ma Nuvvuagittuq supracrustal belt, Canada. *Earth and Planetary Science Letters* **254**, 358-376, doi:10.1016/j.epsl.2006.11.042 (2007).

19 Mloszewska, A. M. *et al.* Chemical sedimentary protoliths in the >3.75Ga Nuvvuagittuq Supracrustal Belt (Québec, Canada). *Gondwana Research* **23**, 574-594, doi:10.1016/j.gr.2012.11.005 (2013).

20 Cates, N. L. & Mojzsis, S. J. Metamorphic zircon, trace elements and Neoarchean metamorphism in the ca. 3.75 Ga Nuvvuagittuq supracrustal belt, Québec (Canada). *Chemical Geology* **261**, 99-114, doi:10.1016/j.chemgeo.2009.01.023 (2009).

21 Edwards, K. J. *et al.* Ultra-diffuse hydrothermal venting supports Fe-oxidizing bacteria and massive umber deposition at 5000 m off Hawaii. *ISME J* **5**, 1748-1758, doi:10.1038/ismej.2011.48 (2011).

22 Juniper, S. K. & Fouquet, Y. Filamentous iron-silica deposits from modern and ancient hydrothermal sites. *Canadian Mineralogist* **26**, 859-869 (1988).

23 Li, J. *et al.* Microbial diversity and biomineralization in low-temperature hydrothermal iron-silica-rich precipitates of the Lau Basin hydrothermal field. *FEMS Microbiology Ecology* **81**, 205-216, doi:10.1111/j.1574-6941.2012.01367.x (2012).

24 Boyd, T. D. & Scott, S. D. Microbial and hydrothermal aspects of ferric oxyhydroxides and ferrosic hydroxides: the example of Franklin Seamount, Western Woodlark Basin, Papua New Guinea. *Geochemical Transactions* **2**, 45, doi:10.1039/b105277m (2001).

25 Emerson, D. & Moyer, C. L. Neutrophilic Fe-oxidizing bacteria are abundant at the Loihi seamount hydrothermal vents and play a major role in Fe oxide deposition. *Applied and Environmental Microbiology* **68**, 3085-3093, doi:10.1128/aem.68.6.3085-3093.2002 (2002).
26 Hein, J. R., Clague, D. A., Koski, R. A., Embley, R. W. & Dunham, R. E. Metalliferous sediment and a silica-hematite deposit within the Blanco Fracture Zone, Northeast Pacific. *Marine Georesources & Geotechnology* **26**, 317-339, doi:10.1080/10641190802430986 (2008).
27 Grenne, T. & Slack, J. F. Bedded jaspers of the Ordovician Løkken ophiolite, Norway: seafloor deposition and diagenetic maturation of hydrothermal plume-derived silica-iron gels. *Mineralium Deposita* **38**, 625-639, doi:10.1007/s00126-003-0346-3 (2003).
28 Little, C. T. S., Glynn, S. E. J. & Mills, R. A. Four-hundred-and-ninety-million-year record of bacteriogenic iron oxide precipitation at sea-floor hydrothermal vents. *Geomicrobiology Journal* **21**, 415-429, doi:10.1080/01490450490485845 (2004).
29 Duhig, N. C., Stolz, J., Davidson, G. J. & Large, R. R. Cambrian microbial and silica gel textures in silica iron exhalites from the Mount Windsor volcanic Belt, Australia: Their petrography, chemistry, and origin. *Economic Geology* **87**, 764-784 (1992).
30 Krepski, S. T., Emerson, D., Hredzak-Showalter, P. L., Luther, G. W., 3rd & Chan, C. S. Morphology of biogenic iron oxides records microbial physiology and environmental conditions: toward interpreting iron microfossils. *Geobiology* **11**, 457-471, doi:10.1111/gbi.12043 (2013).
31 Picard, A., Obst, M., Schmid, G., Zeitvogel, F. & Kappler, A. Limited influence of Si on the preservation of Fe mineral-encrusted microbial cells during experimental diagenesis. *Geobiology*, doi:10.1111/gbi.12171 (2015).
32 Chi Fru, E. *et al.* Biogenicity of an Early Quaternary iron formation, Milos Island, Greece. *Geobiology* **13**, 225-244, doi:10.1111/gbi.12128 (2015).
33 Little, C. T. S., Herrington, R., Haymon, R. & Danelian, T. Early Jurassic hydrothermal vent community from the Franciscan Complex, San Rafael Mountains, California. *Geology* **27**, 167-170 (1999).
34 Ayupova, N. R. & Maslennikov, V. V. Biomorphic textures in the ferruginous-siliceous rocks of massive sulfide-bearing paleohydrothermal fields in the urals. *Lithology and Mineral Resources* **48**, 438-455, doi:10.1134/s0024490213030024 (2013).
35 Sun, Z. *et al.* Generation of hydrothermal Fe-Si oxyhydroxide deposit on the Southwest Indian Ridge and its implication for the origin of ancient banded iron formations. *Journal of Geophysical Research: Biogeosciences* **120**, 187-203, doi:10.1002/2014jg002764 (2015).
36 Ayupova, N. R., Maslennikov, V. V., Sadykov, S. A., Maslennikova, S. P. & Danyushevsky, L. V. in *Biogenic—Abiogenic Interactions in Natural and Anthropogenic Systems* (eds V. Olga Frank-Kamenetskaya, G. Elena Panova, & Yu Dmitry Vlasov) 109-122 (Springer International Publishing, 2016).
37 Campbell, K. A. *et al.* Tracing biosignature preservation of geothermally silicified microbial textures into the geological record. *Astrobiology* **15**, 858-882, doi:10.1089/ast.2015.1307 (2015).
38 Parenteau, M. N. & Cady, S. L. Microbial biosignatures in iron-mineralized phototrophic mats at Chocolate Pots Hot Springs, Yellowstone National Park, United States. *Palaios* **25**, 97-111, doi:10.2110/palo.2008.p08-133r (2010).
39 Thompson, K. J., Lliros, M., Michiels, C., Kenward, P. & Crowe, S. in *2014 GSA Annual Meeting* Vol. 46 401 (Geological Society of America Abstracts with Programs, Vancouver, British Columbia, 2014).
40 Kohler, I., Konhauser, K. O., Papineau, D., Bekker, A. & Kappler, A. Biological carbon precursor to diagenetic siderite with spherical structures in iron formations. *Nature Communications* **4**, 1741, doi:10.1038/ncomms2770 (2013).
41 Sun, Z. *et al.* Mineralogical characterization and formation of Fe-Si oxyhydroxide deposits from modern seafloor hydrothermal vents. *American Mineralogist* **98**, 85-97, doi:10.2138/am.2013.4147 (2012).

42 Heaney, P. J. & Veblen, D. R. An examination of spherulitic dubiomicrofossils in Precambrian banded iron formations using the transmission electron microscope. *Precambrian Research* **49**, 355-372 (1991).
43 Beyssac, O., Goffe, B., Chopin, C. & Rouzaud, J. N. Raman spectra of carbonaceous material in metasediments: a new geothermometer. *Journal of metamorphic geology* **20**, 859–871 (2002).
44 Heimann, A. *et al.* Fe, C, and O isotope compositions of banded iron formation carbonates demonstrate a major role for dissimilatory iron reduction in ~2.5 Ga marine environments. *Earth and Planetary Science Letters* **294**, 8-18, doi:10.1016/j.epsl.2010.02.015 (2010).
45 Cappellen, P. V. & Berner, R. A. A mathematical model for the early diagenesis of phosphorus and flourine in marine sediments: apatite precipitation *American Journal of Science* **288**, 289-333 (1988).
46 Papineau, D. *et al.* Nanoscale petrographic and geochemical insights on the origin of the Palaeoproterozoic stromatolitic phosphorites from Aravalli Supergroup, India. *Geobiology* **14**, 3-32, doi:10.1111/gbi.12164 (2016).
47 Brasier, A. T., Rogerson, M. R., Mercedes-Martin, R., Vonhof, H. B. & Reijmer, J. J. G. A Test of the biogenicity criteria established for microfossils and stromatolites on Quaternary tufa and speleothem materials formed in the ''Twilight Zone'' at Caerwys, UK. *Astrobiology* **15**, 883-900, doi:10.1089/ast.2015.1293 (2015).
48 Zaikin, A. N. & Zhabotinsky, A. M. Concentration wave propagation in two-dimensional liquid-phase self-oscillating system. *Nature* **225**, 535-537 (1970).
49 Smith, A. J. B., Beukes, N. J., Gutzmer, J., Johnson, C. M. & Czaja, A. D. in *Goldschmidt.* 2384 (Mineralogical Society).
50 Walter, M. R., Goode, A. D. T. & Hall, W. D. M. Microfossils from a newly discovered Precambrian stromatolitic iron formation in Western Australia *Nature* **261**, 221-223 (1976).

Methods

1.1 Optical microscopy

Standard 30 μm thick, polished and doubly-polished thin sections and 3mm thick polished slabs were prepared with a final polishing step using Al_2O_3 0.5μm powder for investigation using transmitted and reflected light microscopy. An Olympus BX51 microscope, with 5X, 10X, 20X, 50X and 100X objectives not using immersion oil and CCD camera was used to map petrographic features in thin section. Depth reconstruction images were formed from multiple images taken at 2 micron intervals through thin sections and recombined utilising the Z-project function in the ImageJ software.

1.2 Confocal Raman spectroscopy

Micro-Raman microscopy was conducted on petrographic targets within the polished thin sections using a WiTec alpha300 confocal Raman imaging microscope with a 532nm wavelength laser and operating at a power between 0.1 and 6mW depending on the target. Raman spectra and hyperspectral scans were obtained at variable magnification of 20X to 100X and hence variable spatial resolutions of up to 360nm and spectral resolutions of 4 cm^{-1} were achieved using a 600 lines/ mm grating. Hyperspectral images were created for

specific mineral phases using peak intensity mapping for characteristic peaks of each individual minerals in a scan. Average spectra were calculated by creating a mask on homogeneous pixels of individual phases and had their backgrounds fitted to a polynomial function and subtracted. Large area scans (>100µm x 100µm) were completed using the same process outlined previously, with spatial resolutions below 10µm. Peak parameters were calculated from a Lorenz function modelled for each selected peak. Cosmic ray reduction was applied to all Raman spectra.

1.3 Scanning electron microscopy

Scanning electron microscopy (SEM) in back scattered electron (BSE) and secondary electron (SE) imaging modes was used to characterise the morphology and composition of selected targets, which were also characterised by energy-dispersive x-ray spectroscopy (EDS). Analyses were carried out in the Department of Earth Sciences at University College London using a JEOL JSM-6480L SEM. Standard operating conditions for SEM imaging and EDS analysis were 15kV accelerating voltage, working distance of 10mm, and electron beam current of 1nA. Samples were coated with a few nanometres of Au prior to analysis.

1.4 Electron probe micro-analyser (EPMA)

Major element mineral analyses of minerals were obtained using a JEOL8100 Superprobe (WDS) at Birkbeck College, London. Analysis was carried out using an accelerating voltage of 15kV, current of 1nA, and beam spot diameter of 1µm. The analyses were calibrated against standards of natural silicates, oxides, and Specpure® metals with the data corrected using a ZAF program.

1.5 Focused Ion Beam nano-fabrication

Focused ion beam (FIB) trench milling was performed using a Zeiss 1540 XB FIB-SEM. Targets located by secondary electrons were protected by a 1-µm-thick W shield deposited on the thin section surface. FIB foils were prepared using a focused beam of Ga ions starting with currents of 5nA, going down to 200 and 100pA for the final steps to expose subsurface minerals, before secondary electron images were acquired. Detailed description of the FIB nano-fabrication procedures can be found elsewhere [52,53].

1.6 ICP-MS

Rare earth element analyses were performed by Activation Laboratories Ltd., 41 Bittern Street, Ancaster, Ontario, L9G 4V5, Canada, using a Varian Vista 735 ICP-MS. Yttrium was measured to a detection limit of 2ppm and all other REE have detection limits of 0.1ppm or better.

1.7 LA-ICP-MS

Analyses were conducted at the London Geochronology Centre (LGC), in the Department of Earth Sciences, UCL, utilising an ESI NWR193 laser-ablation system coupled to an Agilent 7700x ICPMS. Instrument parameters are given in tables. S1 and S2. LA-ICPMS procedures followed [54], with Madagascar Apatite (ID-TIMS age 473.5 0.7 Ma; [55]) used as an external age standard for corrections of mass bias and fractionation. Isotopes measured and dwell times are listed in tables S3 and S4. Glitter 4.4 [56] was used for data reduction; ages were calculated following [57], where the calculated $^{206}Pb/^{238}U$ age was used for grains younger than 1100 Ma, and the $^{207}Pb/^{206}Pb$ age for older grains, rejecting analyses exhibiting more than +5/-15% discordance. Trace element concentrations were calculated using NIST SRM 612 and 610 glass [58,59] as external standards; ^{44}Ca was used as internal standard, assuming stoichiometric concentration for apatite.

LA-ICP-MS instrument parameters

RF power 1340 W
Ar Carrier Gas ow 1.04 l/min
He gas ow 950 ml/min
Sweep Time 400 / 900 ms (U-Pb / trace elements)

Table.S1 Laser Ablation parameters

Wavelength	193 nm Pulse
duration	20 ns Energy
fluency	2.5 J/cm2
Ablation spot size	25 µm
Pulse repetition rate	10 Hz
Ablation time / spot	25 / 30 s (U-Pb / trace elements)

Table.S2 Acquired masses for U-Pb dating. 235U was ommitted, natural 238U/235U ratio of 137.88 is assumed.

Mass	Element	Dwell time
29	Si	5ms
43	Ca	5ms
44	Ca	5ms
206	Pb	100ms
207	Pb	200ms
208	Pb	100ms
221	bkg	5ms
232	Th	100ms
238	U	100ms

Table.S3 Acquired masses for trace elements.

Mass	Element	Dwell time
23	Na	5ms
27	Al	5ms
29	Si	5ms
43	Ca	5ms
44	Ca	5ms
55	Mn	10ms
88	Sr	50ms
89	Y	50ms
137	Ba	50ms
139	La	50ms
140	Ce	50ms
141	Pr	50ms
146	Nd	50ms
147	Sm	50ms
153	Eu	50ms
157	Gd	50ms
159	Tb	50ms
163	Dy	50ms
165	Ho	50ms
166	Er	50ms
169	Tm	50ms
172	Yb	50ms
175	Lu	50ms
221	background	5ms

Extended data reference

51 Bolhar, R., Kamber, B. S., Moorbath, S., Fedo, C. M. & Whitehouse, M. J. Characterisation of early Archaean chemical sediments by trace element signatures. *Earth and Planetary Science Letters* **222**, 43-60, doi:10.1016/j.epsl.2004.02.016 (2004).

Methods references

52 Wirth, R. Focused Ion Beam (FIB) combined with SEM and TEM: Advanced analytical tools for studies of chemical composition, microstructure and crystal structure in geomaterials on a nanometre scale. *Chemical Geology* **261**, 217-229, doi:10.1016/j.chemgeo.2008.05.019 (2009).

53 Zega, T. J., Nittler, L. R., Busemann, H., Hoppe, P. & Stroud, R. M. Coordinated isotopic and mineralogic analyses of planetary materials enabled by in situ lift-out with a focused ion beam scanning electron microscope. *Meteoritics and Planetary Science* **42**, 1-14 (2007).

54 Jackson, S. E., Pearson, N. J., Griffin, W. L. & Belousova, E. A. The application of laser ablation-inductively coupled plasma-mass spectrometry to in situ U{Pb zircon geochronology. *Chemical Geology* **211**, 47-69 (2004).

55 Chew, D. M., Sylvester, P. J. & Tubrett, M. N. U-Pb and Th-Pb dating of apatite by LA-ICPMS. *Chemical Geology* **280**, 200-216 (2011).

56 Griffin, W. L., Powell, W. J., Pearson, N. J. & O'Reilly, S. Y. in *Laser Ablation-ICP-MS in the Earth Sciences: Current Practices and Outstanding Issues* Vol. 40 (ed P.J Sylvester) 308-311 (2008).

57 Ludwig, K. R. User' s Manual for Isoplot 3.70. *Berkeley Geochronology Center Special Publication* **76** (2008).

58 Reed, W. P. Certificate of Analysis, Standard Reference Materials 612 and 613. *Tech. Rep., National Institute of Standards & Technology.* (1992).

59 Jochum, K. P. *et al.* Determination of Reference Values for NIST SRM 610-617 Glasses Following ISO Guidelines. *Geostandards and Geoanalytical Research* **35**, 397-429 (2011).

Supplementary data references

60 Mills, R. A., Clayton, T. & Alt, J. C. Low-temperature fluid flow through sulfidic sediments from TAG: modification of fluid chemistry and alteration of mineral deposits. *Geophysical research letters* **23**, 3495–3498 (1996).

61 Alt, J. C. Hydrothermal oxide and nontronite deposits on seamounts in the eastern Pacific. *Marine Geology* **81**, 227-239 (1988).

62 Mills, R. A., Elderfield, H. & Thomson, J. A dual origin for the hydrothermal component in a metalliferous sediment core from the Mid-Atlantic Ridge. *Journal of Geophysical research* **98**, 9671-9681 (1993).

63 Grenne, T. & Slack, J. F. Paleozoic and Mesozoic silica-rich seawater: Evidence from hematitic chert (jasper) deposits. *Geology* **31**, 319-322 (2003).

64 Grenne, T. & Slack, J. F. Geochemistry of Jasper Beds from the Ordovician Løkken Ophiolite, Norway: Origin of Proximal and Distal Siliceous Exhalites. *Economic Geology* **100**, 1511-1527 (2005).

65 O'Neil, J., Boyet, M., Carlson, R. W. & Paquette, J.-L. Half a billion years of reworking of Hadean mafic crust to produce the Nuvvuagittuq Eoarchean felsic crust. *Earth and Planetary Science Letters* **379**, 13-25, doi:10.1016/j.epsl.2013.07.030 (2013).

66 David, J., Godin, L., Stevenson, R., O'Neil, J. & Francis, D. U-Pb ages (3.8-2.7 Ga) and Nd isotope data from the newly identified Eoarchean Nuvvuagittuq supracrustal belt, Superior Craton, Canada. *Geological Society of America Bulletin* **121**, 150-163, doi:Doi 10.1130/B26369.1 (2009).

67 Turner, S., Rushmer, T., Reagan, M. & Moyen, J. F. Heading down early on? Start of subduction on Earth. *Geology* **42**, 139-142, doi:10.1130/g34886.1 (2014).

68 Franklin, J. M., Gibson, H. L., Jonasson, I. R. & Galley, A. G. in *Economic Geology: One Hundredth Anniversary Volume* (eds J.W Hedenquist, J.F.H Thompson, R.J Goldfarb, & J.P Richards) 523-560 (The Economic Geology Publishing Company, 2005).

69 Cates, N. L. & Mojzsis, S. J. Pre-3750 Ma supracrustal rocks from the Nuvvuagittuq supracrustal belt, northern Québec. *Earth and Planetary Science Letters* **255**, 9-21, doi:10.1016/j.epsl.2006.11.034 (2007).

70 Boily, M., Leclair, A., Maurice, C., Bédard, J. H. & David, J. Paleo- to Mesoarchean basement recycling and terrane definition in the Northeastern Superior Province, Québec, Canada. *Precambrian Research* **168**, 23-44, doi:10.1016/j.precamres.2008.07.009 (2009).

71 Augland, L. E. & David, J. Protocrustal evolution of the Nuvvuagittuq Supracrustal Belt as determined by high precision zircon Lu–Hf and U–Pb isotope data. *Earth and Planetary Science Letters* **428**, 162-171, doi:10.1016/j.epsl.2015.07.039 (2015).

72 Roth, A. S. G. *et al.* Inherited 142Nd anomalies in Eoarchean protoliths. *Earth and Planetary Science Letters* **361**, 50-57, doi:10.1016/j.epsl.2012.11.023 (2013).

73 Klein, C. Some Precambrian banded iron-formations (BIFs) from around the world: Their age, geologic setting, mineralogy, metamorphism, geochemistry, and origins. *American Mineralogist* **90**, 1473-1499, doi:10.2138/am.2005.1871 (2005).
74 Miyano, T. & Klein, C. Phase equilibria in the system K20 - FeO - MgO - AIzO3 - SiO2 - H20 - CO2 and the stability limit of stilpnomelane in metamorphosed Precambrian iron-formations. *Contributions to Mineralogoy and Petrology* **102**, 478-491 (1989).
75 Garcıa-Ruiz, J. M. *et al.* Self-assembled silica-carbonate structures and detection of ancient Microfossils. *Science* **302**, 1194-1197 (2003).
76 Stone, D. A. & Goldstein, R. E. Tubular precipitation and redox gradients on a bubbling template. *Proceedings of the national academy of science* **101**, 11537-11541, doi:10.1073/pnas.0404544101 (2004).
77 Hopkinson, L., Roberts, S., Herrington, R. & Wilkinson, J. Self-organization of submarine hydrothermal siliceous deposits: Evidence from the TAG hydrothermal mound, 26N Mid-Atlantic ridge. *Geology* **26** (1998).
78 Li, J. *et al.* Microbial diversity and biomineralization in low-temperature hydrothermal iron-silica-rich precipitates of the Lau Basin hydrothermal field. *FEMS Microbiology Ecology* **81**, 205-216, doi:10.1111/j.1574-6941.2012.01367.x (2012).
79 Parenteau, M. N. & Cady, S. L. Microbial Biosignatures in Iron-Mineralized Phototrophic Mats at Chocolate Pots Hot Springs, Yellowstone National Park, United States. *Palaios* **25**, 97-111, doi:10.2110/palo.2008.p08-133r (2010).
80 Zhou, X. *et al.* Biogenic Iron-Rich Filaments in the Quartz Veins in the Uppermost Ediacaran Qigebulake Formation, Aksu Area, Northwestern Tarim Basin, China: Implications for Iron Oxidizers in Subseafloor Hydrothermal Systems. *Astrobiology* **15**, 523-537, doi:10.1089/ast.2014.1234 (2015).
81 Slack, J. F., Grenne, T., Bekker, A., Rouxel, O. J. & Lindberg, P. A. Suboxic deep seawater in the late Paleoproterozoic: Evidence from hematitic chert and iron formation related to seafloor-hydrothermal sulfide deposits, central Arizona, USA. *Earth and Planetary Science Letters* **255**, 243-256, doi:10.1016/j.epsl.2006.12.018 (2007).
82 Barghoorn, E. S. & Tyler, S. A. Microorganisms from Gunflint Chert - These Structurally Preserved Precambrian Fossils from Ontario Are Most Ancient Organisms Known. *Science* **147**, 563-&, doi:DOI 10.1126/science.147.3658.563 (1965).
83 Shapiro, R. S. & Konhauser, K. O. Hematite-coated microfossils: primary ecological fingerprint or taphonomic oddity of the Paleoproterozoic? *Geobiology* **13**, 209-224, doi:10.1111/gbi.12127 (2015).
84 Kinnunen, K. A. Primary sedimentary features in Kittila jasper, Finnish Lapland. *The geological society of Finland bulletin* **54**, 69-76 (1982).
85 Karkhanis, S. N. Fossil iron bacteria may be preserved in Precambrian feroan carbonate. *Nature* **261**, 406-407 (1976).
86 Laberge, G. L. Possible Biological Origin of Precambrian Iron-Formations. *Economic Geology* **68**, 1098-1109 (1973).
87 Winter, B. L. & Knauth, L. P. Stable isotope geochemistry of cherts and carbonates from the 2.0 Ga Gunflint Iron Formation: implications for the depositional setting, and the effects of diagenesis and metamorphism. *Precambrian Research* **59**, 283-313 (1992).
88 Carrigan, W. J. & Cameron, E. M. Petrological and stable isotope studies of carbonate and sulfide minerals from the Gunflint Formation, Ontario: evidence for the origin of early Proterozoic iron-formation. *Precambrian Research* **52**, 347-380 (1991).
89 Rasmussen, B., Meier, D. B., Krapez, B. & Muhling, J. R. Iron silicate microgranules as precursor sediments to 2.5-billion-year-old banded iron formations. *Geology* **41**, 435-438, doi:10.1130/g33828.1 (2013).
90 Sun, Z. *et al.* Mineralogical characterization and formation of Fe-Si oxyhydroxide deposits from modern seafloor hydrothermal vents. *American Mineralogist* **98**, 85-97, doi:10.2138/am.2013.4147 (2012).
91 Peng, X. *et al.* Intracellular and extracellular mineralization of a microbial community in the Edmond deep-sea vent field environment. *Sedimentary Geology* **229**, 193-206, doi:10.1016/j.sedgeo.2010.06.003 (2010).
92 Knoll, A. H. & Barghoor, E. S. Ambient Pyrite in Precambrian Chert: New Evidence and a Theory. *Proceedings of the national academy of science* **71**, 2329-2331 (1974).
93 Klein, C. & Fink, P. R. Petrology of the Sokoma Iron Formation in the Howells R iver area, at the western edge of the Labrador trough. *Economic Geology* **71**, 453-487 (1976).
94 Ayres, D. E. Genesis of Iron-bearing Minerals in Banded Iron Formation Mesobands in The Dales Gorge Member, Hamersley Group, Western Australia. *Economic Geology* **67**, 1214-1233 (1972).
95 Ahn, J. H. & Buseck, P. R. Hematite Nanospheres of Possible Colloidal Origin from a Precambrian Banded Iron Formation. *Science* **250**, 111-113, doi:DOI 10.1126/science.250.4977.111 (1990).
96 Ribeiro da Luz, B. & Crowley, J. K. Morphological and chemical evidence of stromatolitic deposits in the 2.75Ga Carajás banded iron formation, Brazil. *Earth and Planetary Science Letters* **355-356**, 60-72, doi:10.1016/j.epsl.2012.08.028 (2012).

Main text figure legends

Figure 1. Transmitted light images of haematite filaments from the NSB (A, C-E) and Løkken jaspers (B). A. Filaments attached to a terminal knob (arrow) coated by nanoscopic haematite. B. Filaments in the Løkken jaspers coated by nanoscopic haematite and attached to terminal knobs (red arrows) and branching (orange arrows). Inset of multiple

filaments attached to a terminal knob. C. Filaments in quartz band; haematite rosettes (green arrow). Inset of branching filament (orange arrow). D. Filament enveloped in haematite (inset is the same image in cross polars). E. Filament attached to iron-oxide band and coated with haematite.

Figure 2. Transmitted light images of haematite tubes in the NSB (A-F) and Løkken jaspers (G-H). A. Tubes associated with iron-oxide band. B. Depth reconstruction of tubes with haematite filament (arrow). Inset image of tubes at the surface. C. Tube showing filament (red arrow) and walls (black arrow). D. Strongly deformed tubes. E. Depth reconstruction of tubes. F. Two tubes attached to terminal knob (arrows); lower image taken in false colour. G. Tube with haematite filament. H. Aligned tubes (green arrows).

Figure 3. Carbonate rosettes from the NSB. A. TL image of calcite rosettes. B. Area targeted by Raman in C. D. Raman filter map at 1580 cm^{-1} (width 40cm^{-1}) with spectra of graphite particles circled. E. TL + Cross-polar image of calcite rosettes. F. TL image of target area shown in G. White arrow shows apatite cutting a carbonate rosette; red arrow shows apatite inclusions in a carbonate rosette. H. CM Raman filter map at 1565cm^{-1} (width 50cm^{-1}). I. and J. Selected average Raman spectra from maps and CM.

Figure 4. Granules from the Biwabik and NSB jaspers. A. Cross-polar image of granules in Biwabik jasper with Raman map in B. C. Cross-polar image of granule in the NSB with Raman map in D. E and F. Selected average Raman spectra of CM and minerals from maps.

Extended Data Figure legends

Fig E1. A-D Field photos of the NSB BIF outcrops. A. Bands of magnetite and chert. B. Jasper (top red layer) in contact with Fe-rich carbonate (bottom grey layer). C. Layered jaspers with meta-volcanic layers. D. Layered jasper; dominantly bands of grey haematite and haematitic chert. E. Field location, local geology and sample locations

Fig E2. Rare Earth Element (REE) Post-Archean Australian shale normalized plots. A. LA-ICP-MS REE measurements in apatite from PC0844. B. Jasper bulk rock REE; PC0824 (dark grey) and PC0844 (light grey). NSB (red[15] and green[16]) and Isua[51] (blue) BIF bulk rock REE.

Fig E3. Thin sections of samples in this study (see supplementary information for localities). Red boxes mark haematite tubes and tube-like structures. Red arrow highlights the orientation of tubes. Blue circle highlights concretion structure in thin section and slab. Numbering of targets corresponds to figures. Inset in E shows transmitted light image of CM inside apatite lath. Inset in F shows reflected light image of small, sub-spherical chalcopyrites with haematite. All sections are 2.5 cm wide, except rock slab (A) measuring 7x2 cm and Løkken-Høydal (K-O) dimensions are 2x6cm, except JAH samples which measure 2x8cm.

Fig E4. Photomicrographs taken in plane polarised light with reflected light of haematite tubes and filaments. Images in left column are taken at surface of the thin section. Images in right column show a series of stacked images using Z-project function in ImageJ. Stacked images are formed of 8-9 sequential images taken at 2 µm intervals through the thin section. A. Branching haematite filament. B. Stacked image of A. Arrows points to loose coiling. C. Hollow tube truncated partially at the surface showing both the top (red arrow) and D. bottom surface (black arrow) of the tube. E. Twisted haematite filaments emanating from haematite knob at varying angles and depth through the thin section. Inset shows aligned haematite crystals in filament indicative of twisting; arrow points to three tightly aligned plates. F. Stacked image of E. with insets of candidate twisted stalks formed of aligned haematite plates; arrows show twist points. Dashed red boxes

correspond to area of insets. G. Filament diameter measurements from NSB (blue) and Løkken-Høydal (orange) jaspers. Filament diameters for NSB: *n* = 23, Std Dev = 2.8, Avg = 8.3 and for Løkken-Høydal: *n* = 28 Std Dev=1.9, Avg=9.1. H. Tube diameters *n* = 40, Std Dev = 6.3, Avg = 24.9 for both NSB and *n* = 40 Std Dev = 3.1, Avg = 19.5 Løkken-Høydal.

Fig. E5. Carbonate-apatite and CM in the NSB and Løkken jaspers in association with haematite filaments. A-B. Tl and Raman image of carbonate associated with CM inside a filament mat. C-D. Tl and Raman image of carbonate associated with graphite in the NSB jasper associated with a filament. E. Contextual image of the carbonate grain (red box) with haematite filaments. F. Raman spectra of minerals mapped in this figure. G. Contextual image of carbonate grain (red box) with haematite filaments. H-I. Tl and Raman image of haematite filament in Løkken jasper, associated with apatite and carbonate grains. J-K Tl and Raman image of haematite filament in NSB jasper associated with carbonate grains (green circles). L. Contextual image of apatite associated with CM and carbonate within millimetres of filaments in the Løkken jasper. M-N. Tl and Raman image of apatite grain. O. Contextual image of graphite in carbonate spatially occurring within millimetres of haematite filaments and apatite in the NSB. P-Q Tl and Raman image of graphite particle in carbonate. R. Raman spectra of CM in Løkken jaspers from figures B and N. S. Raman spectra of CM in NSB jaspers from figures D and Q

Fig E6. Carbonate rosettes. A TL image of calcite rosettes from the NSB. B-C. TL and Raman image of target area. D. Graphite Raman filter map (Filter: 1580cm^{-1}, width 40cm^{-1}). Circled pixels are graphite grains. E. Raman spectra of selected graphite particles. F. Average Raman spectra for Raman map in C; with inset of haematite Raman filter map (Filter: 1320cm^{-1}, width 30cm^{-1}). Circled pixels are haematite grains. G. Stilpnomelane laths overgrowing apatite in the NSB. H. Ankerite rhombohedra envelop a layer of CM in the Dales Gorge Member of the Brockman IF. I. Ankerite rosettes, with quartz inclusions in a CM layer. J. Ankerite rosette with quartz core from the Løkken jasper. K. Ankerite rosettes overgrowing haematite filaments and corresponding Raman map. L. Selected carbon spectra showing diversity of carbon preservation. Non-graphitized carbon is the most abundant variety in the rosettes. M. Average Raman spectra from map.

Fig E7. TL+RL images of haematite rosettes in NSB (A-D) and Løkken (E) jaspers. A. Large (60 µm) haematite rosettes with cores. B. Haematite rosettes in dense haematite. C. Deformed, thicker walled (25 µm) haematite rosettes (arrows). D. Concentric haematite rosette. E. Haematite rosettes from Løkken jaspers, same scale bar for all.

Fig E8. Variety of graphitic carbons from the NSB. A. TL image of graphitic carbon particles from PC0822. B. Secondary electron image, looking down a Focused Ion Beam trench through graphitic carbon particles. C. Raman spectral map of A. D. Raman spectra for phases in spectral map. E. 1. Disordered graphitic carbon in apatite lath, TL. 2. Disordered graphitic carbon in a granule, TL. 3. Poorly crystalline graphitic carbon vein, TL. 4. Crystalline graphitic carbon in a carbonate rosette, TL. F. Raman spectra showing the transition between haematite and CM. The 1320 cm^{-1} haematite peak produces a disordered CM spectrum. However, the G-peak position shows such CM is not disordered CM like immature kerogen with peaks around 1610 cm^{-1}. A Raman map at 330nm resolution shows the section (green line) across which the Raman spectra were taken. Note the inclusions of haematite (pink) in the CM (red). All other colours and mineral spectra for the Raman map are in Fig. E9G.

Fig E9. Granules from the NSB and from the Løkken jaspers. A. TL image of a granule in the NSB. B. Raman map of granule A. C. CM Raman filter map (Filter: 1580 cm^{-1}, width 80 cm^{-1}). D. Calcite Raman filter map (Filter: 1089 cm^{-1}, width 20 cm^{-1}). E. Apatite Raman filter map (Filter: 965 cm^{-1}, width 30 cm^{-1}). F. 1 µm spatial resolution Raman scan of part of granule A. G.

360 nm resolution Raman scan of part of G (yellow and white colours are colour combination artefacts). H. 500 nm resolution Raman scan of a portion of the interior of the Mary Ellen granule in Fig. 4B, showing CM coating a carbonate grain, like CM coating a carbonate grain in the NSB granule A. I. Granule from the Løkken jasper, TL . J. Granule in I, viewed in CP light. Note the characteristic internal quartz recrystallization, relative to the matrix. K. Raman map of granule in I. Note that magnetite forms a rim around the granule like the NSB and Biwabik granules (Fig.5). L. Microfossil within a granule preserved in haematite. The morphology shows the characteristic terminal knob of iron like the larger tubes preserved in the NSB. M. CM Raman filter map (Filter: 1566 cm^{-1}, width 60 cm^{-1}). N. Average Raman spectra for all Raman maps in this figure. O. Representative CM spectra from granules in this figure. P-Q. CP images of iron-bearing granules from the Mary Ellen (Biwabik) and NSB IFs showing relative quartz recrystallization and magnetite rims.

Figure 1.

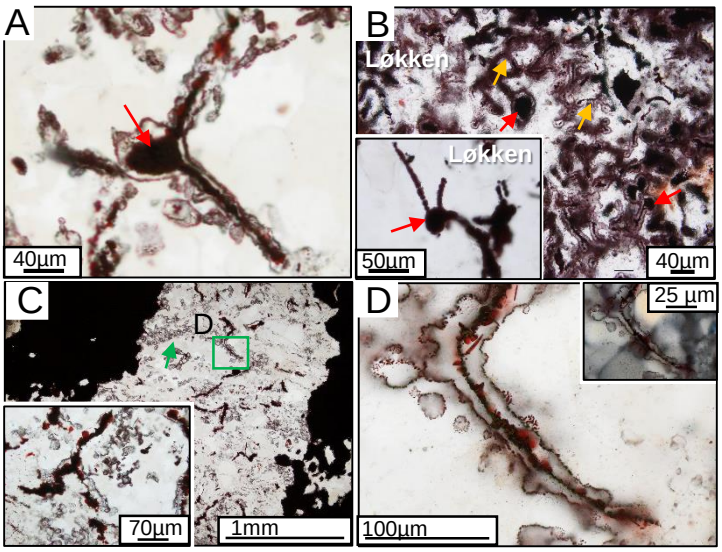

Figure 2.

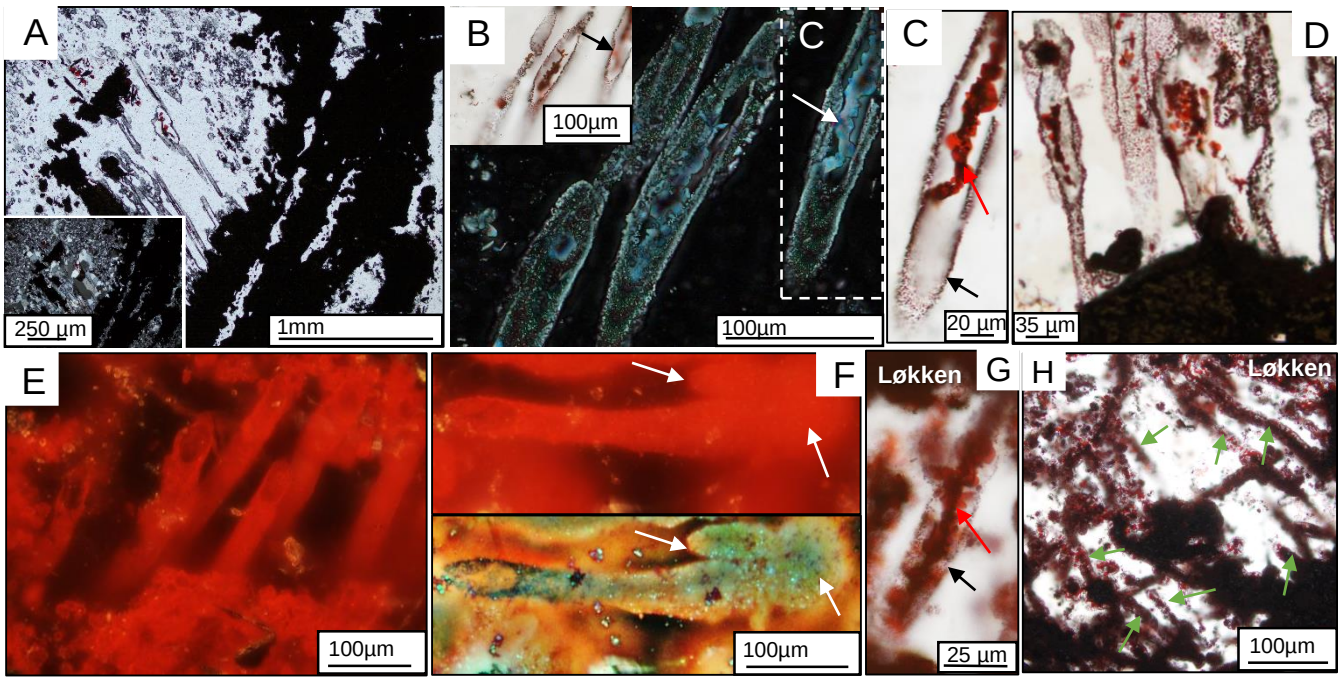
A
250 µm
1mm
B
100µm
C
100µm
C
20 µm
D
35 µm
E
100µm
F
100µm
Løkken
G
25 µm
H
Løkken
100µm

Figure 3.

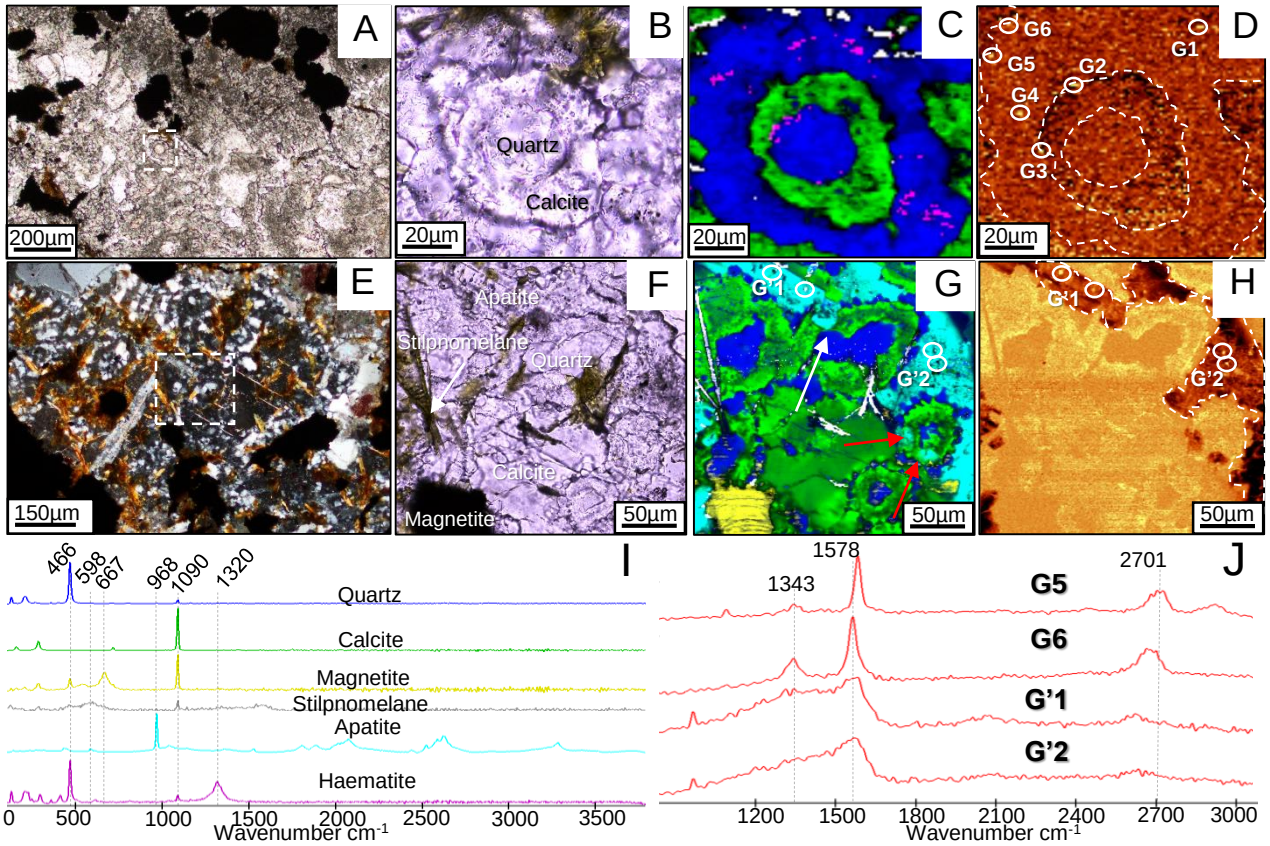
A
200µm
B
Quartz
Calcite
20µm
C
20µm
D
G6
G5
G2
G1
G4
G3
20µm
E
150µm
F
Apatite
Stilpnomelane
Quartz
Calcite
Magnetite
50µm
G
G1
G'2
50µm
H
G'1
G'2
50µm
I
466
598
667
968
1090
1320
Quartz
Calcite
Magnetite
Stilpnomelane
Apatite
Haematite
0
500
1000
1500
2000
2500
3000
3500
Wavenumber cm-1
J
1578
1343
2701
G5
G6
G'1
G'2
1200
1500
1800
2100
2400
2700
3000
Wavenumber cm-1

Figure 4.

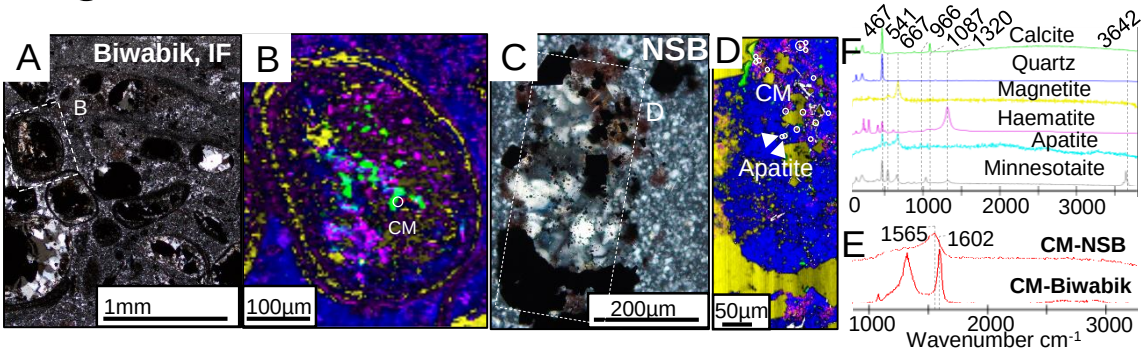
A
Biwabik, IF
B
1mm
B
CM
100µm
C
NSB
D
200µm
D
CM
Apatite
50µm
F
467
541
667
966
1087
1320
3642
Calcite
Quartz
Magnetite
Haematite
Apatite
Minnesotaite
0
1000
2000
3000
E
1565
1602
CM-NSB
CM-Biwabik
1000
2000
3000
Wavenumber cm-1


A


B


C


D

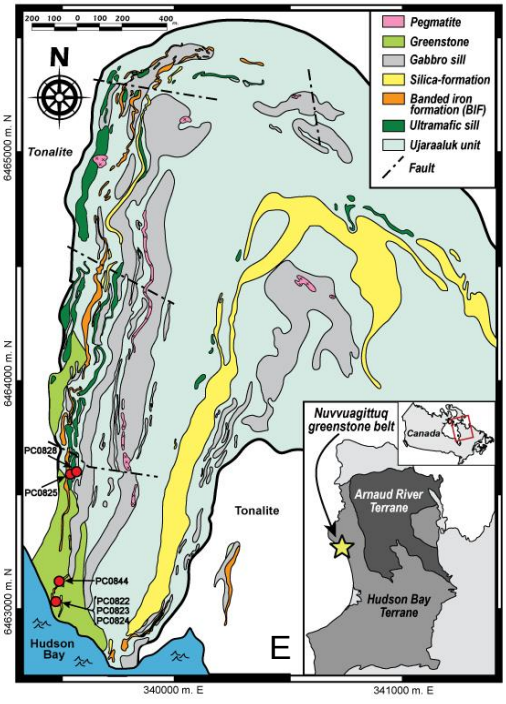
200 100 0 100 200 400 m
N
Pegmatite
Greenstone
Gabbro sill
Silica-formation
Banded iron formation (BIF)
Ultramafic sill
Ujaraaluk unit
Fault
Tonalite
6465000 m. N
6464000 m. N
6463000 m. N
PC0828
PC0825
PC0844
PC0822
PC0823
PC0824
Hudson Bay
Tonalite
Nuvvuagittuq greenstone belt
Canada
Arnaud River Terrane
Hudson Bay Terrane
E
340000 m. E
341000 m. E

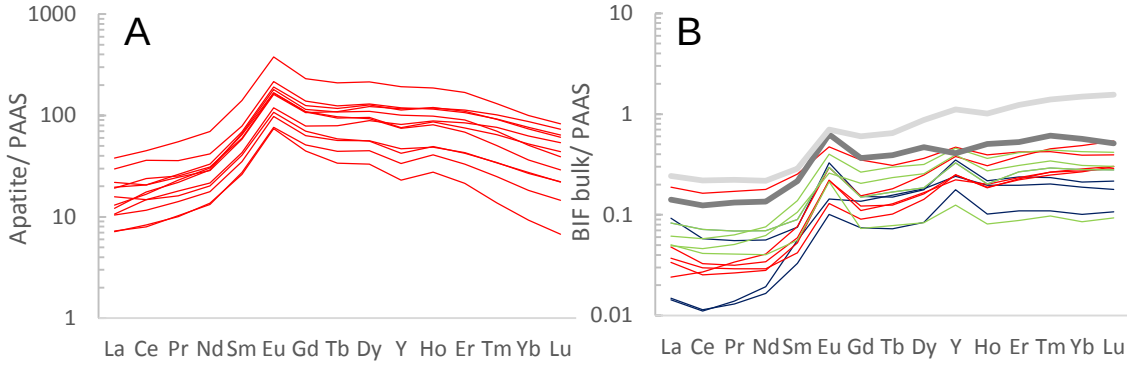
A
1000
100
10
1
Apatite/ PAAS
La Ce Pr Nd Sm Eu Gd Tb Dy Y Ho Er Tm Yb Lu
B
10
1
0.1
0.01
BIF bulk/ PAAS
La Ce Pr Nd Sm Eu Gd Tb Dy Y Ho Er Tm Yb Lu

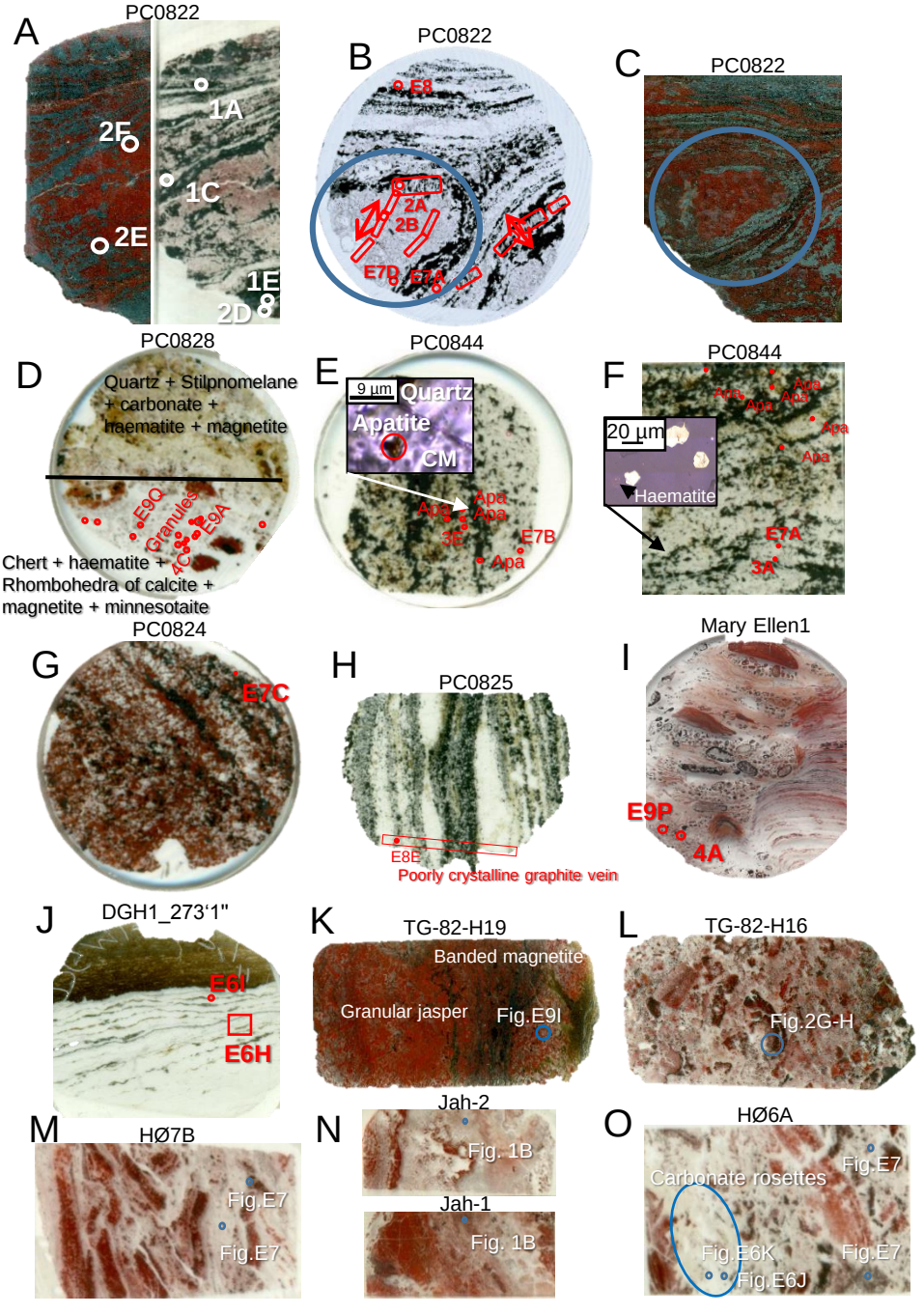
A
PC0822
2F
1A
1C
2E
1E
2D
B
PC0822
E8
2A
2B
E7D
E7C
C
PC0822
D
PC0828
Quartz + Stilpnomelane + carbonate + haematite + magnetite
E9Q
Granules
E9A
Chert + haematite + Rhombohedra of calcite + magnetite + minnesotaite
E
PC0844
9 µm
Quartz
Apatite
CM
Apa
3C
E7B
F
PC0844
20 µm
Haematite
E7A
3A
G
PC0824
E7C
H
PC0825
E8E
Poorly crystalline graphite vein
I
Mary Ellen1
E9P
4A
J
DGH1_273'1"
E6I
E6H
K
TG-82-H19
Banded magnetite
Granular jasper
Fig.E9I
L
TG-82-H16
Fig.2G-H
M
HØ7B
Fig.E7
Fig.E7
N
Jah-2
Fig. 1B
Jah-1
Fig. 1B
O
HØ6A
Carbonate rosettes
Fig.E7
Fig.E6K
Fig.E6J
Fig.E7

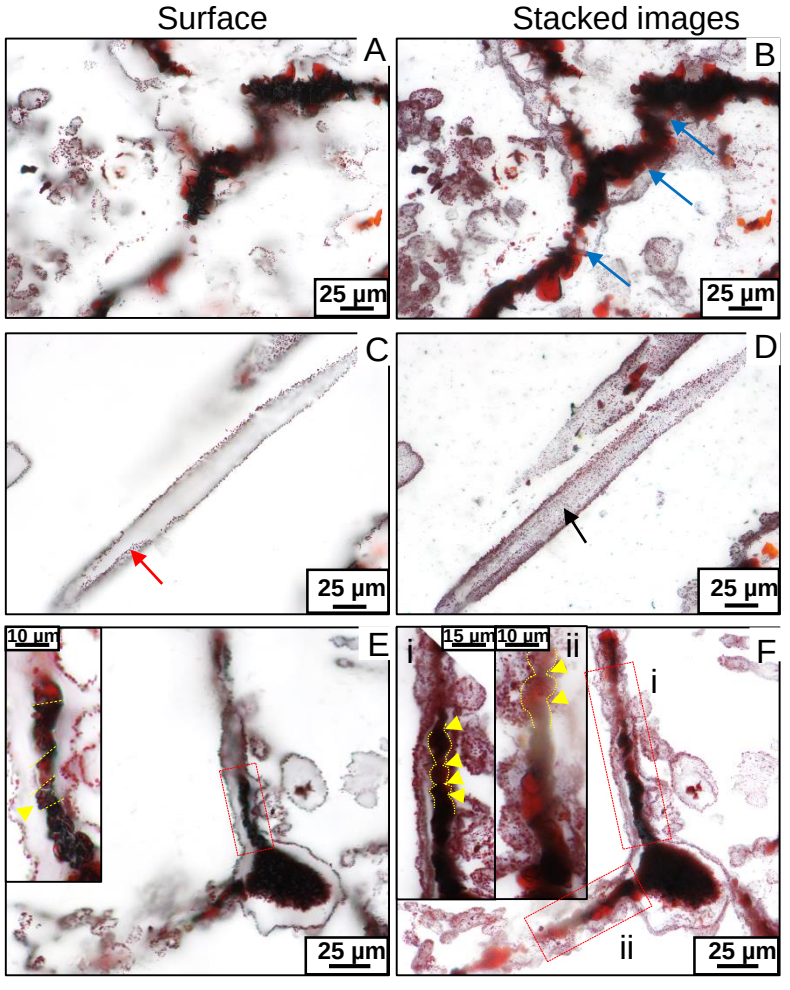
Surface
Stacked images
A
B
C
D
E
F
25 µm
10 µm
15 µm
i
ii

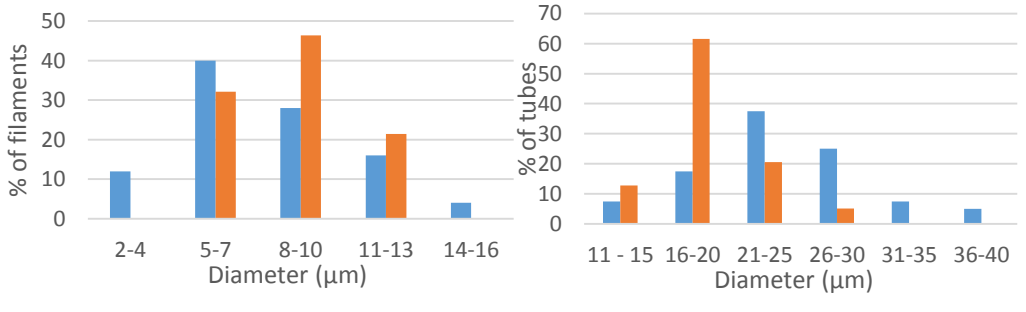
% of filaments
50
40
30
20
10
0
2-4
5-7
8-10
11-13
14-16
Diameter (µm)
% of tubes
70
60
50
40
30
20
10
0
11 - 15
16-20
21-25
26-30
31-35
36-40
Diameter (µm)

Løkken

NSB

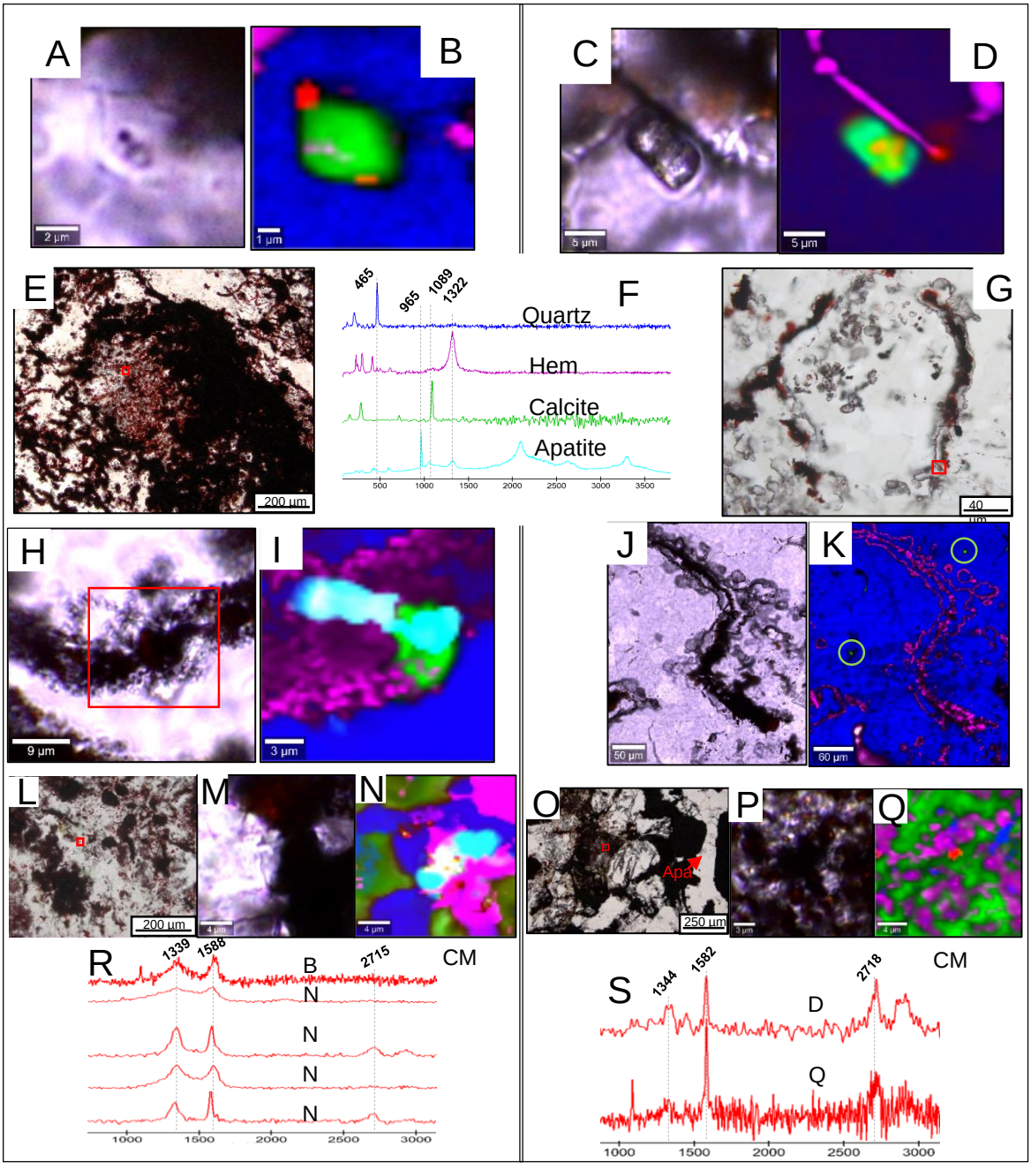
A
B
2 µm
1 µm
C
D
5 µm
5 µm
E
200 µm
465
965
1089
1322
F
Quartz
Hem
Calcite
Apatite
500
1000
1500
2000
2500
3000
3500
G
40
H
9 µm
I
3 µm
J
50 µm
K
60 µm
L
200 µm
M
4 µm
N
4 µm
O
Apa
250 µm
P
3 µm
Q
4 µm
R
1339
1588
2715
B
N
N
N
N
CM
1000
1500
2000
2500
3000
S
1344
1582
2718
D
Q
CM
1000
1500
2000
2500
3000

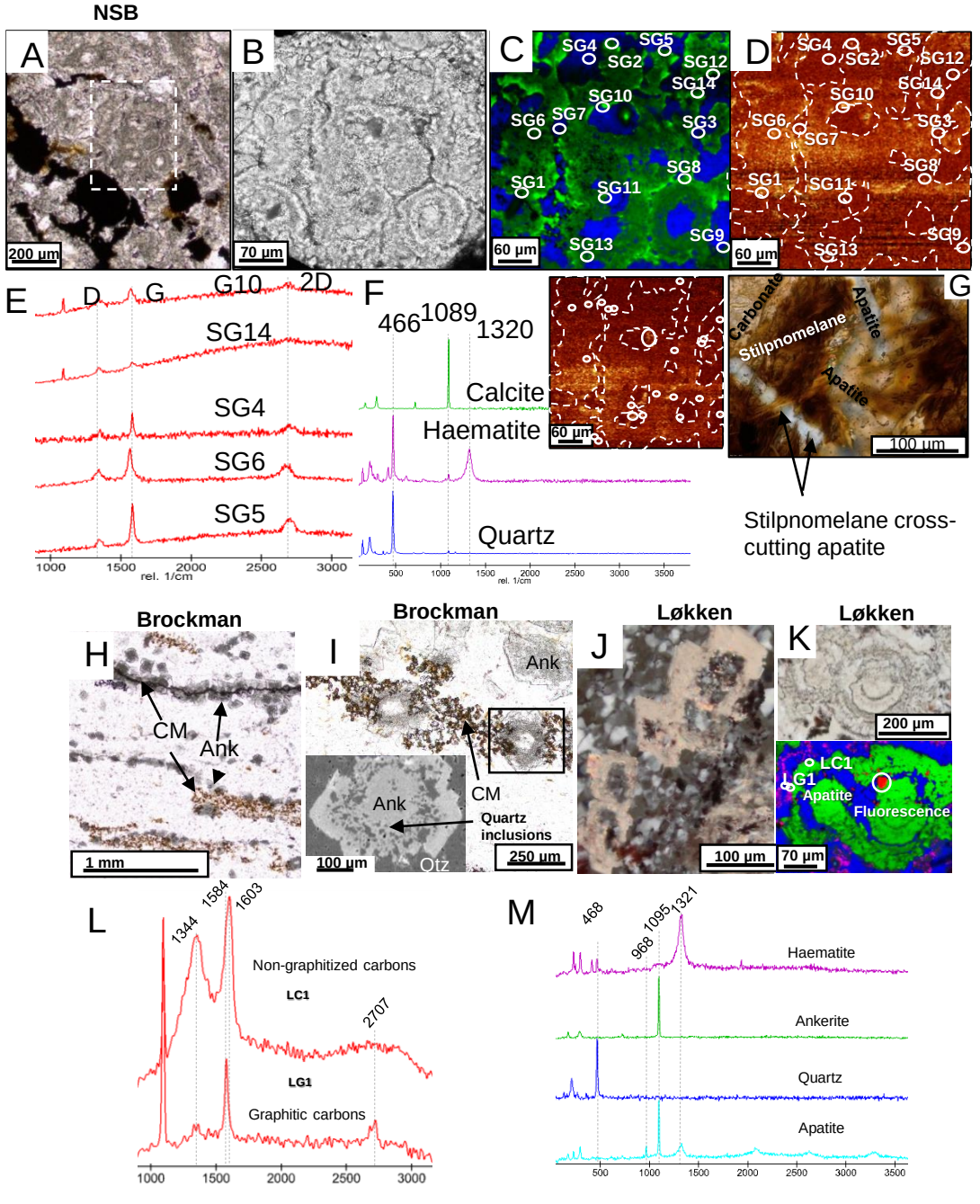
NSB
A
B
C
D
200 µm
70 µm
60 µm
60 µm
SG1
SG2
SG3
SG4
SG5
SG6
SG7
SG8
SG9
SG10
SG11
SG12
SG13
SG14
E
D
G
G10
2D
SG14
SG4
SG6
SG5
1000
1500
2000
2500
3000
rel. 1/cm
F
466
1089
1320
Calcite
Haematite
Quartz
60 µm
500
1000
1500
2000
2500
3000
3500
rel. 1/cm
G
Carbonate
Stilpnomelane
Apatite
Apatite
100 µm
Stilpnomelane cross-cutting apatite
Brockman
Brockman
Løkken
Løkken
H
CM
Ank
1 mm
I
Ank
CM
Ank
Quartz inclusions
100 µm
Qtz
250 µm
J
100 µm
K
200 µm
LC1
LG1
Apatite
Fluorescence
70 µm
L
1344
1584
1603
2707
Non-graphitized carbons
LC1
LG1
Graphitic carbons
1000
1500
2000
2500
3000
M
468
968
1095
1321
Haematite
Ankerite
Quartz
Apatite
500
1000
1500
2000
2500
3000
3500

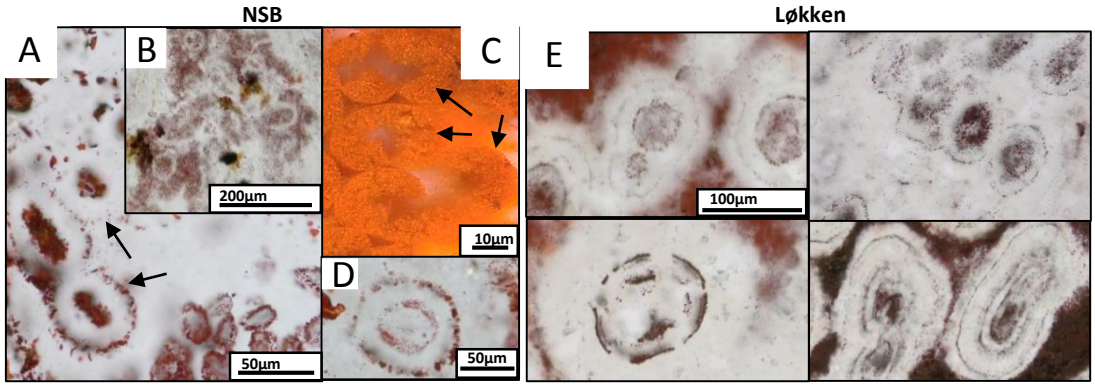
NSB
Løkken
A
B
C
D
E
200µm
50µm
10µm
50µm
100µm

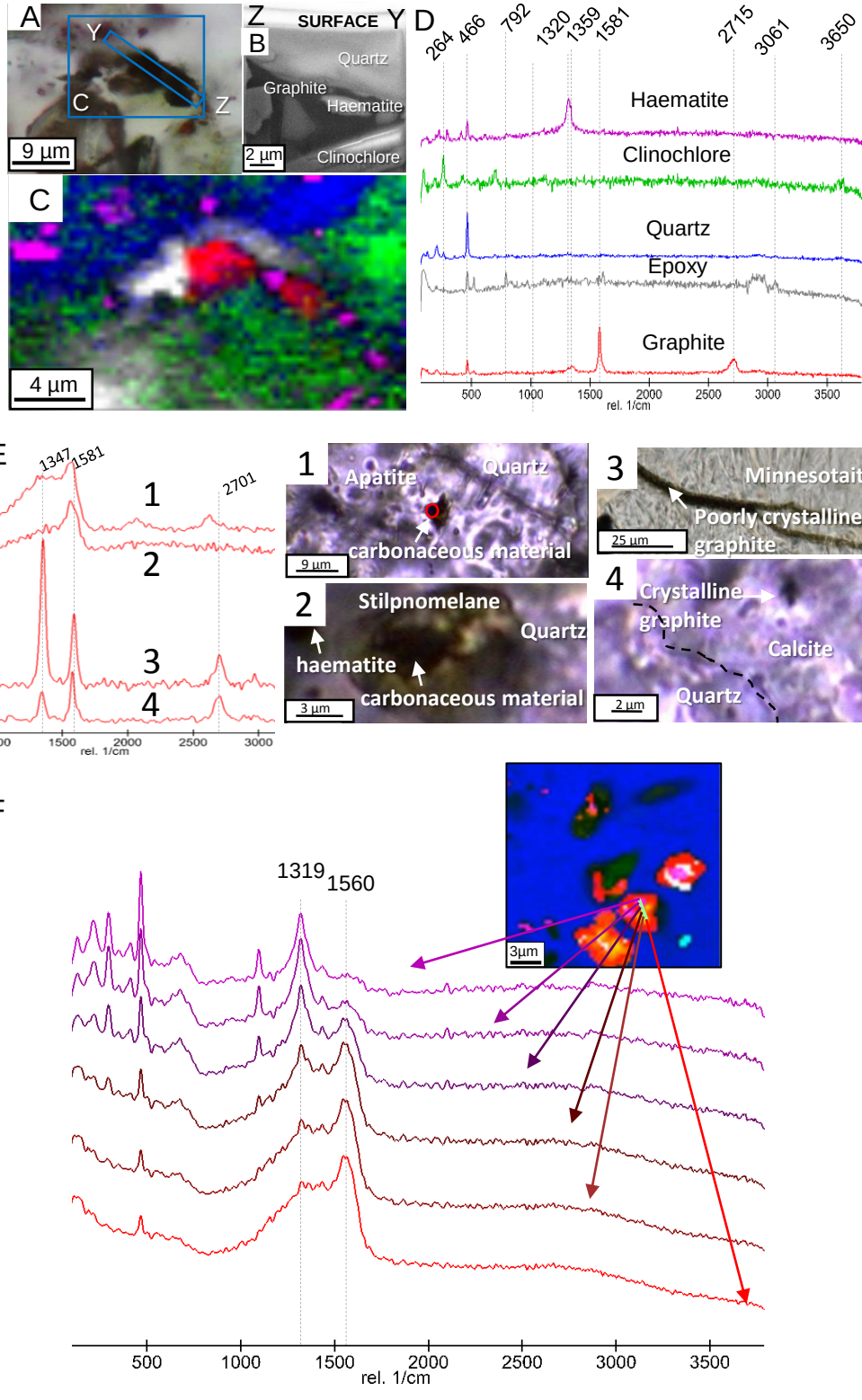
A
Y
C
Z
9 µm
Z
SURFACE
Y
B
Quartz
Graphite
Haematite
2 µm
Clinochlore
C
4 µm
D
264
466
792
1320
1359
1581
2715
3061
3650
Haematite
Clinochlore
Quartz
Epoxy
Graphite
500
1000
1500
2000
2500
3000
3500
rel. 1/cm
E
1347
1581
2701
1
2
3
4
1000
1500
2000
2500
3000
rel. 1/cm
1
Apatite
Quartz
carbonaceous material
9 µm
2
Stilpnomelane
Quartz
haematite
carbonaceous material
3 µm
3
Minnesotaite
Poorly crystalline graphite
25 µm
4
Crystalline graphite
Calcite
Quartz
2 µm
F
1319
1560
3µm
500
1000
1500
2000
2500
3000
3500
rel. 1/cm

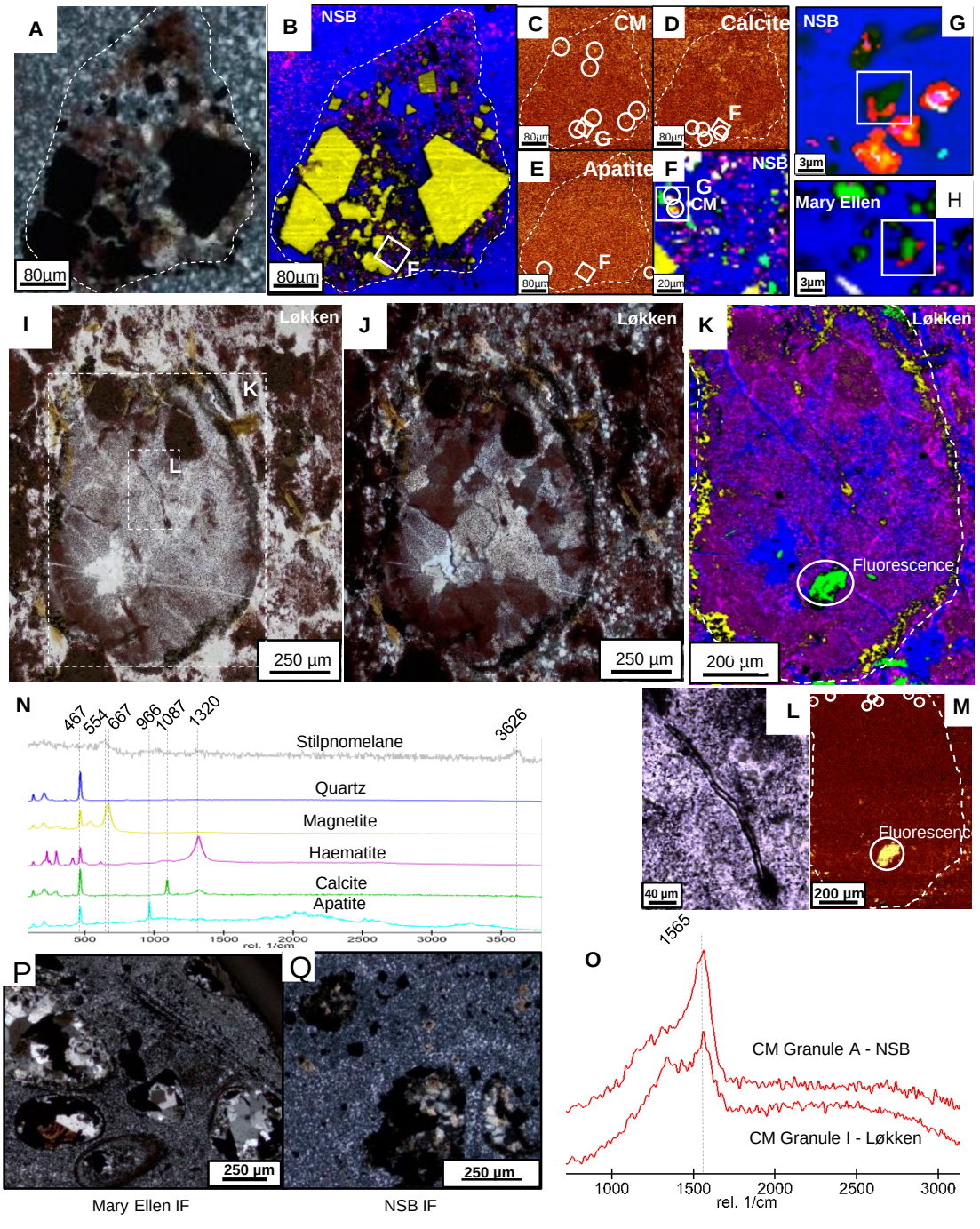
A
80µm
B
NSB
F
80µm
C
CM
G
80µm
D
Calcite
F
80µm
E
Apatite
F
80µm
F
NSB
G
CM
20µm
NSB
G
3µm
Mary Ellen
H
3µm
I
Løkken
K
L
250 µm
J
Løkken
250 µm
K
Løkken
Fluorescence
200 µm
N
467
554
667
966
1087
1320
3626
Stilpnomelane
Quartz
Magnetite
Haematite
Calcite
Apatite
500
1000
1500
2000
2500
3000
3500
rel. 1/cm
L
40 µm
M
Fluorescenc
200 µm
P
250 µm
Q
250 µm
Mary Ellen IF
NSB IF
O
1565
CM Granule A - NSB
CM Granule I - Løkken
1000
1500
2000
2500
3000
rel. 1/cm

Jaspers of the Løkken ophiolite

Jaspers are typically bedded cherts (silica-rich, microcrystalline rocks) rich in haematite ± magnetite ± Fe-silicate minerals. Stratiform occurrences of jasper with pillow basalts and volcanogenic massive sulphide deposits imply an origin from lithified hydrothermal precipitates [21,27,29], formed in submarine settings analogous to those of modern mid-ocean ridges or back-arc sea-floor spreading centres, intra-plate seamounts, or flanks and calderas of arc volcanoes [22,23,26]. Si-Fe colloidal-gel protoliths of jaspers can be attributed to several processes, including *in situ* precipitation from low-temperature (20-100°C [60]) fluid flow through oceanic crust [61], material derived from low-temperature (2-50°C) vent chimneys [61], and proximal or distal sedimentation from hydrothermal plumes [62].

The Early Ordovician (Tremadoc) Løkken ophiolite was deformed and emplaced during the Caledonian orogeny, reaching metamorphic grades of lower greenschist facies; the original setting was dominated by back-arc rifting in a marginal basin [63]. The ophiolite contains laterally extensive jaspilitic beds that cluster at stratigraphic levels equivalent to those of the Løkken and Høydal volcanogenic massive sulphide (VMS) deposits and are in places intimately associated with the Fe-Cu-Zn sulphide ore. The jasper, which formed originally as sea-floor gels, displays myriad exceptionally well-preserved primary textures, including haematitized bacteria remains, haematitic tubes, and a variety of textures attributed to gel maturation and more advanced diagenetic changes [63]. The gel was deposited by particle fallout from hydrothermal plumes, in which silica flocculation and rapid settling of colloidal particles was promoted by the bridging effect of Fe oxyhydroxide [27]. Fe was sourced from white smoker-type vents with high Fe/S ratios [64], whereas silica is thought to be primarily of ambient seawater origin based on the interpretation of silica saturation or supersaturation in pre-Late Cretaceous oceans [27]. Trace element variations in the gel precursor were controlled by coprecipitation and/or adsorption by Fe oxyhydroxide particles within the plume(s), REE patterns (positive Eu and negative Ce anomalies) reflect mixing of hydrothermal solutions with seawater at dilution ratios of ~10^2 to 10^4.

The Nuvvuagittuq Supracrustal belt (NSB)

The NSB is located in the Northeastern Superior Province, in northern Québec, Canada. It is surrounded and intruded by multiple generations of Eoarchaean to Palaeoarchaean tonalite-trondhjemite-granodiorite (TTG) gneisses dated at 3760 Myr, 3660 Myr, 3500 Myr, and 3350 Myr [65,66], and forms a core enclave within the Neoarchaean TTG gneisses of the Inukjuak domain. The NSB is dominated by mafic amphibolites composed of cummingtonite-plagioclase-biotite±garnet[17].

The amphibolite unit has been interpreted to represent mafic volcanic deposits, with compositions ranging from basaltic to basaltic andesite [11]. In some locations, pillow lava structures are preserved within the amphibolite [11]. These amphibolites are divided into three geochemical groups displaying distinct Al/Ti ratios and following a chemo-stratigraphy within the NSB [11].The base of the sequence is characterised by low Al/Ti

metabasaltic rocks with tholeiitic affinities. They exhibit relatively flat trace element profiles and their chemistry is consistent with derivation from an undepleted mantle source and fractionation under relatively dry conditions [11]. The top of the stratigraphy comprises amphibolites having geochemical compositions consistent with derivation from a re-enriched depleted mantle and fractionation under elevated water pressure [11]. They comprise high Al/Ti basaltic amphibolite relatively depleted in incompatible trace elements and displaying characteristic concave-up REE profiles typical of modern boninites. They are overlaid by intermediate Al/Ti amphibolite of basaltic to andesitic compositions with calc-alkaline affinities displaying LREE-enrichments and flat HREE profiles. Chemical sedimentary rocks (BIF and chert-like silica rocks) mark the transition in the stratigraphy between the low Al/Ti tholeiitic amphibolite and the higher Al/Ti boninitic and calc-alkaline amphibolite. This transition and chemo-stratigraphy led some to suggest that the NSB metavolcanic rocks were formed in subduction initiation settings similar to those of modern convergent tectonic settings [67]. Locally, the NSB amphibolite is composed of a cordierite-orthoamphibole mineral assemblage and is characterised by high Mg and K concentrations with depleted Ca, Na, and Si. This mineralogical assemblage and geochemical signature are consistent with seawater hydrothermal alteration of the oceanic crust [68]. Together with the presence of pillow lavas and BIF, this pattern suggests that the NSB formed through submarine volcanism with important hydrothermal activity.

On the basis of mineralogy, two broad types of BIF lithologies are recognized from the NSB including quartz + ferrous silicates (banded silicate formation (BSF) and quartz + magnetite + ferrous silicates (BIF) [16]. Other minor lithologies that have been identified in the belt are jasper-quartz-carbonate, quartz-biotite schists (with possible meta-conglomerates), and chromite-bearing silica rock [69, 12, 18, 19].

Outcrops of BIF vary from 5 to 30m in thickness, with the jasper forming thinner beds of 1 m thickness and less, commonly interbedded with layers of amphibolite. In places, small veins, typically a few cm wide of jasper infiltrate and cut the amphibolite [19], suggesting Fe-Si gels infilled networks within the (interpreted) pyroclastics during deposition. The depositional depth of the NSB jaspers is uncertain from the associated lithologies or textures in rocks of the belt; however, the occurrence of fine-scale, iron-oxide lamination (Fig. E3A) is similar to that in other younger jaspers and IFs suggestive of a calm depositional environment below wave base.

The NSB was mostly metamorphosed to upper amphibolite facies with temperatures reaching 650 °C and 4-5 Kbar [17, 20]. Sm-Nd isotopic compositions of garnets in the NSB amphibolites suggest that the peak metamorphic event occurred in the Neoarchaean [14] contemporaneous with intrusion of pegmatites dated at 2688 ± 2 Myr [66]. This is also consistent with the regional metamorphism occurring at 2705–2680 Myr [70]. The amphibolites in the southwest and southeast corners of the NSB are characterised by lower metamorphic grade assemblages of chlorite+epidote+actinolite. To the southeast, chlorite preserves the shape of what appears to have been garnet crystals, suggesting that the lower greenschist assemblage is retrograde [17]. No evidence of retrogressed garnet is observed in the lower grade facies to the southwest, which may never have reached upper amphibolite facies. Very local layers in Fe-cherts preserve primary chert, calcite rhombohedra, and well-formed minnesotaite needles in jasper, suggesting some rare layers escaped severe recrystallisation during peak metamorphism. Furthermore, the crystallisation temperatures estimated for graphitic carbon in rocks from the southwest corner of the NSB do not exceed 550°C (Table S9-10), suggesting that the metamorphic facies did not exceed much past greenschist facies.

The geochronology of the NSB is highly debated and two ages have been proposed for the contained metavolcanic rocks: an Eoarchaean age of ~3750 Myr [69] and a Hadaean age of ~4280 Myr [15]. Here we present an overview of this geochronological debate.

One of the challenges in precisely dating the formation of the NSB is the quasi-absence of zircon-bearing felsic rocks and their equivocal relationship to the mafic metavolcanic rocks. Rare bands of felsic rocks with trondhjemitic composition have yielded zircons dated by U-Pb between 3750 and 3774 Myr [69, 66, 65, 13, 71]. These trondjhemitic rocks consist of thin discontinuous bands 25-40 cm in width found only at the southern edge of the NSB [17]. Other interpretations placed these rocks as felsic intrusions due to cross-cutting relationships observed in the field [69], thus giving a minimum age for the NSB. Other field evidence such as the presence of felsic intrusions within gabbro sills were used to reach to the same conclusion about their intrusive nature [14,65]. Other works, however, interpreted these rocks as felsic volcanites [71], hence providing the actual age for the NSB. Significantly, this is inconsistent with the cross-cutting relationships observed by [69]. Fuchsitic quartz-rich rocks in the NSB have been interpreted as detrital quartzites by some works [12] which yielded 13 zircons with $^{207}Pb/^{206}Pb$ ages ranging from 3718 Myr to 3780 Myr. These therefore put a maximum age for the NSB at 3780 Myr. However, this interpretation is inconsistent with the principle of inclusion, because the maximum age for the detrital quartzite should be constrained by the youngest 3718 Myr detrital zircon. This, however, is in conflict with the minimum age of 3770 Myr for the NSB supported by the age of the cross-cutting felsic rocks [69]. Other studies ascertained the same U-Pb age of 3794 ± 16 Myr for the fuchsitic rocks, which they conversely interpreted as metasomatically altered felsic orthogneiss of intrusive origin [13], hence providing a minimum age for the NSB. A Hadaean age for the NSB is supported by the ^{142}Nd isotopic composition of the mafic amphibolites. ^{142}Nd is the daughter product of ^{146}Sm, and because the parent isotope has a short half-life of 103 Myr, any deviation in ^{142}Nd compared to modern terrestrial standards implies Sm-Nd fractionation before ca. 4000 Myr, prior to extinction of ^{146}Sm. A significant number of NSB amphibolites exhibit anomalous ^{142}Nd compositions compared to modern terrestrial standards. The correlation

between the $^{142}Nd/^{144}Nd$ and Sm/Nd ratios for all three groups of NSB amphibolite is interpreted by some [14,15] to represent an isochron giving an igneous age of ca. 4290 Myr for the NSB metavolcanic rocks. This Hadaean age has been challenged by some who interpreted the $^{142}Nd/^{144}Nd$ vs. Sm/Nd correlation to reflect mixing with a Hadaean-enriched reservoir [72]. However, this correlation is preserved between the mafic amphibolite and their ultramafic co-genetic cumulates, which can be used to argue against mixing as a cause of the $^{142}Nd/^{144}Nd$ vs. Sm/Nd correlation [14]. The composition of these ultramafic rocks is controlled by olivine fractionation and they are interpreted to be co-genetic cumulates to the mafic amphibolites [11]. The $^{142}Nd/^{144}Nd$ vs. Sm/Nd correlation between the hypothesised mafic liquids and ultramafic cumulates can only be produced if the igneous fractionation occurs while ^{146}Sm was still decaying, i.e. prior to 4000 Myr. A Hadaean age for the NSB is also supported by the ^{147}Sm-^{144}Nd isotopic composition of intruding gabbro sills that yield an isochron age of ca. 4100 ± 100 Myr, which would establish a minimum age for the NSB metavolcanic rocks [14].

Hence, there is still no consensus on the exact age of the NSB, but nonetheless, it is at least 3770 Ma and possibly as old as 4290 Myr, which makes the NSB BIF among the oldest, if not the oldest, chemical sedimentary rocks known on Earth.

Jaspers and BIFs metamorphosed at the upper greenschist/ lower amphibolite facies

Eoarchaean supracrustal belts worldwide are generally metamorphosed to at least upper amphibolite facies. The metamorphic mineral assemblages of BIFs are well-documented [73]. Petrographic and quantitative analysis of elements in Fe-silicate minerals within BIFs can be used to constrain metamorphic facies. In the BIFs of the NSB, the highest-grade samples exhibit extensive recrystallization and dissemination of coarse magnetite layers, and contain fayalite and pyroxene that indicate amphibolite- to granulite-facies conditions. With decreasing grades, the BIFs lack fayalite and instead contain minor pyroxene, amphiboles (predominantly grunerite-cummingtonite), and retrograde phyllosilicates (clinochlore). The low-grade BIFs contain patches of fine and coarse grained quartz. The very lowest grade BIFs have acicular stilpnomelane, minnesotaite, and rhombohedral ferroan calcite (Fig. E3D). The stilpnomelane in lower grade BIF is likely prograde, because this mineral does not form massive pseudomorphs after higher grade minerals, but rather fine euhedral laths. An upper stability field of 430-470°C and 5-6 Kbar is proposed for stilpnomelane [74]. Furthermore, the presence of chert suggests that the P-T conditions of these prograde stilpnomelane--bearing samples did not exceed much past upper greenschist facies.

Null hypothesis and abiotic formation of haematite tubes and filaments

The null hypothesis in the context of early life studies requires one to assess the likelihood of plausible abiotic explanations for observations purporting to support a biological phenomenon. If all plausible abiotic explanations are considered and assessed to be significantly unlikely, then one can reject the null hypothesis leaving a biological interpretation for the observed features. Below we consider the possible abiogenic mechanisms that could have created haematite tubes and filaments akin to those documented in the NSB.

First, the NSB tubes rarely branch, are commonly straight, and exhibit parallel orientation that may reflect preferred mineral growth. If iron was remobilised along crystal boundaries of acicular minerals as they grew during diagenesis and metamorphism, tube-like structures of haematite could have formed. However, if the precursor was not opal then the mineral would need to have been replaced completely, because only quartz is found inside the tubes. Secondly, acicular mineral growth in rocks is not uniform in shape, in contrast to the consistent morphology observed for the tubes.

Likewise, metamorphic processes may elongate quartz-hosted haematite to produce aligned, tubular structures like the tubes in the NSB, through fluctuating volume change in the rock during silica remobilisation or metamorphic stretching. Such processes would lead to the structures and minerals in the local environment being preferentially and consistently aligned, yet the orientation of ribbons and tubes of nanoscopic haematite (Fig. 1C) in the NSB jasper is highly variable over scales from hundreds of microns to millimetres. However, the presence of 500-µm gaps in iron-oxide layers (Fig. E3B) showing strong alignment of tubes and ribbons of haematite raises the possibility that during metamorphism elevated strain pressure pried apart these iron-oxide layers, which subsequently were infilled with silica and haematite that nucleated on the iron-oxide layers and were elongated during continued layer separation. In addition, layers and pre-existing amorphous structures of haematite may have, under pressure, undergone a process similar to neurulation, whereby layers of haematite are pressed together to form tubes. The two mechanisms above could, in theory, form consistently sized tubes in the range of 16-30 µm by reaching a critical size limit, but it is highly unlikely that such mechanisms can facilitate the growth of multiple tubes from a single haematite knob at varying angles (Fig. 1A, E4), both horizontally and vertically during prograde metamorphism, together with the formation of internal filaments and similarly coiled, branched, and twisted filaments (Fig. E4) with delicate haematite envelopes (Fig. 1C). In addition, their close spatial association with carbonate and graphite (Fig. E5D) is most compelling and consistent with a biogenic origin for these tubes and filaments.

Because formation of the NSB tubes via the above metamorphic processes fails to fully explain the NSB tubular structures as metamorphic products, a primary origin of the tubular structures is considered more probable. Nonetheless, there still exist exotic processes that may produce pseudo-microfossils under certain conditions [75]. However, these known exotic processes form filaments of silica and barium carbonate and form under very alkaline conditions, which are unlikely to be relevant for the sea-floor environment of deposition of the NSB jaspers (which lack barite) and formation of the contained tubes. Similar iron-oxide tubes like those present in the NSB have been synthesised using iron-ammonium-sulphate solutions and electric currents, or via mixing

of hydrogen with ammonia bubble streams [76]. Notably, these synthesised tubes are demonstrably different from those in the NSB and younger jaspers. Firstly, the experimental tubes have solid walls of iron oxide and consist of a complex mixture of Fe minerals that vary depending on the nature of the bubble solution, whereas the NSB tube walls are composed only of dispersed, individual, nanoscale grains of haematite, consistent with the recrystallization of primary Fe-oxyhydroxide precipitates from seawater. Secondly, the experimental tubes are variable in size, which contrasts with the generally consistent size of the NSB tubes; yet, a number of tubes in the NSB jasper are strongly deformed and display irregular forms and sizes (Fig. 2D). Finally, the synthesised tubes lack internal chains of platy haematite or any other phase, unlike the NSB tubes.

Whereas tubular structures in modern and lithified hydrothermal precipitates are interpreted almost exclusively as microfossils, some branching filaments have been attributed to inorganic, self-organized mineral growth of Fe-oxyhydroxide, controlled by redox fronts in a silica gel [77]. However, such structures are highly branching and are not reported to occur as tubes, but instead as solid Fe-oxyhydroxide filaments, and hence are debated in terms of biological origin [28]. Similarly, Fe- oxyhydroxide filaments could form abiogenically in a Fe-Si gel and then be coated subsequently by colloidal silica and Fe-oxyhydroxide to form tubes with internal filaments, like those observed in the NSB. However, this process fails to explain the tubes that lack internal filaments, because silica has never been proven to replace haematite, and fails to explain their associations with carbonate and CM; thus, the tubes are unlikely to have formed via this process. Rather, in our interpretation, silica precipitated on and replaced bacterial filaments, which were then coated with nanoscale Fe-oxyhydroxide to form the tubes, while minor amounts of microbial organic matter from the filaments was oxidised to carbonate that are now preserved as carbonate-graphite associations with the filaments (Fig. E5). In summary, the NSB haematite tubes and filaments cannot be explained fully by any known abiotic mechanism, and in light of their association with multiple, independent lines of evidence supporting biological activity, the simple uniting explanation is that these tubes and filaments represent fossilised microbial remains.

Table. S4 List of samples and their locations and methods used in this study

Formation	Samples	Age	General rock type	Optical microscopy	Raman microscopy	SEM/ EPMA	FIB	LA-ICP-MS	Samples locations	
									Northings	Eastings
Løkken ophiolite, Høydal jaspers, Norway	HO6A, HO7B, TG-82-S6, TG-82-H19 and H16, Jah-1 and 2	0.485 Ga	Jasper	X	X	X			Mine tailings	
Animike, Mesabi range, Biwabik Iron Formation, USA	MARY-ELLEN1	1.8 Ga	Stromatolitic jasper	X	X				Mine tailings	
Brockman formation, Dales gorge group, Australia	DGH1_273'1"	2.5 Ga	BIF/ Fe-cherts	X	X	X			DGH1 drill core	
NSB	PC0822, PC0823, PC0824	>3.77 Ga	BIF/ jasper	X	X	X	X	X	58 16 50.9	77 44 14.7
	PC0825								58 17 08.7	77 44 12.2
	PC028/ A								58 17 09.1	77 44 10.8
	PC0844								58 16 53.8	77 44 14.1

Table S5. Iron-oxide tubes and filaments

Locality	Age	Host rock	Diameter Length	Mineralogy	Additonal	Reference
Lau hydrothermal basin, Pacific ocean	Present day	Fe-Si hydrothermal vent sediments	0.5-1.5µm 10-100µm	Iron-oxide-silica	Straight, helical and curved varieties. Core of filaments iron-oxide coated by amorphous silica	78
Chocolate pot hot springs, Yellowstone, USA	Present day	Iron-rich hydrothermal springs	1.5µm >100µm	Ferrihydrite	Very low Total organic carbon present in buried microbial mats	79
Southwest Indian Ridge, Indian Ocean	Present day	Fe-Si oxyhydroxide	2-10µm 10-100µm	Ferrihydrite	Filaments can be curved and intertwining or form bundles of rod-like filaments with the same orientations, diameter and length	80
Franklin Seamount, Woodlark Basin, Papua New Guinea	Present day	Fe-Si-Mn oxyhydroxides	0.5-5µm	Iron-oxide-silica	Filaments have hollow structure with walls of iron oxyhydroxide. Filaments branch and some occur as orientated parallel to one another	24
Various ophiolites and modern day vent sites	Late Jurassic to present day	Inter-pillow cherts, jasper, Fe-Si seafloor gels and inactive chimney fragments	1-10 µm	Iron-oxide-silica-pyrite-barite		22
Numerous deposits	490 Ma to Present day	Japsers	1.2-30 µm 20-3000 µm	haematite-iron-oxide	See tables 1, 2 and 3 in Little et al., 2014. Tubes with internal platy haematite chains (Løkken deposit)	28
Qigebulake Formation, Northwestern Tarim Basin, China	551–541 Ma	Hydrothermal quartz veins	1-5 µm 20-200 µm	Goethite-haematite	No organic carbon detected by Raman	80
Jerome mining district, central Arizona, USA	1738 Ma	Jasper-IF-VMS	1-3 µm 30-50 µm	haematite		81
Frere formation, Australia	1880 Ma	Jasper/ IF	Tubes 4-9 µm Filament 0.5-2 µm 100s µm	Nanoscale haematite	Filaments orientated parallel to oncolites	50
Gunflint iron-formation, North America	1880 Ma	Jasper/ IF	0.5-8 µm Can exceed 300 µm	Nanoscale haematite	Same filament morphologies in other areas of the formation are preserved by organic matter	82,83
Kittilä jaspers, Finland	ca. 2000 Ma	Jasper	?	Nanoscale 'dusty' haematite		84
Hamersley BIF, Dales gorge member, Australia	2500 Ma	BIF (haematite + quartz + magnetite + stilpnomelane + ankerite + minnesotaite + riebeckite)	5 µm 100 µm	haematite-dolomite	Filaments preserved as carbonate moulds attached to iron spheres	85
Nuvvuagittuq supracrustal belt, Canada (filaments)	3750 Ma	Jasper (haematite + quartz + magnetite + ripidolite + chalcopyrite ± calcite ± apatite)	1-7 µm 35-500 µm	Platy-haematite, acicular, grey haematite, moulds in massive nanoscale haematite	Filaments commonly encapsulated by nanoscale haematite. Some have a forked-end. Others exhibit branching	This study
Nuvvuagittuq supracrustal belt, Canada (tubes)	3750 Ma	Jasper (haematite + quartz + magnetite + ripidolite + calcite + chalcopyrite + apatite)	20-30 µm 80-300 µm	Nanoscale haematite	Some contain a central chain of platy haematite	This study

Table S6. Carbonate rosettes in IFs

Locality	Age	Host rock	Diameters	Carbonate	Additional	Reference
Høydal, Norway	480 Ma	Jaspers associated with VMS deposits	100-250 µm	Ankerite	Form circular and rhombohedra rosettes, overgrow haematite filaments; can contain inclusions of CM and associated with apatite	26; This study
Gunflint iron-formation, North America	1880 Ma	Jasper/ IF	20-40 µm	Siderite	Associated with CM and sometimes contain cores of apatite	85, 86, 41, 87
Hamersley BIF, Dales gorge member, Australia	2500 Ma	BIF (haematite + quartz + magnetite + stilpnomelane + ankerite + minnesotaite + riebeckite)	100-300 µm	Ankerite-siderite	Generally rhombohedral in shape, with poikiloitic textures developing, which form a sphere-shaped centre. Associated with CM layers	This study
			60-80 µm	Dolomite-ankerite	Sometimes have a rosette structure in the middle	88
Nuvvuagittuq supracrustal belt, Canada	>3770 Ma	BIF (Calcite + quartz + magnetite + stilpnomelane + haematite + apatite + chalcopyrite)	20-180µm	Fe-calcite	Poikiolitic, rosettes generally rounded, associated with apatite, can contain inclusions of CM and haematite	This study 18

Table S7. Iron-oxide rosettes

Locality	Age	Host rock	Diameters	Mineralogy	Additional	Reference
Lau hydorthermal basin, Pacific ocean	Present day	Fe-Si hydorthermal vent sediments	0.1-2 µm	Si-Ferrihydrite	Associated branching filaments	90, 23
Edmond vent field, Indian ocean	Present day	Inner surface of sulphide chimney	1 µm	Non-crystalline silica and acicular iron oxides	Mineralized cells, with cytoplasm preserved	91
Milos, Greece	2Ma	Hydrothermal vent iron-formation	30 µm	haematite	Associated filaments, crumpled cores	33
Lokken-Hoydal, Norway	480Ma	Jaspers associated with VMS deposits	10-100 µm	haematite-quartz	Forms mm thick layers, large diversity, haematite cores, multi-layered varieties	27
Mount Windsor, Australia	ca. 485Ma	Jaspers associated with VMS deposits	100 µm	haematite-quartz	Multi-layered varieties	29
Frere formation, Australia	1850 Ma	Jasper/ IF	20-50 µm	haematite-quartz	haematite cores and associated haematite filaments	This study
Gunflint iron-formation, North America	1880 Ma	Jasper/ IF	3-30 µm	haematite-quartz		82, 86
Sokoman formation, Canada	1900 Ma	Jasper	3-25 µm	haematite-quartz		86, 92, 93
Great Slave group	Paleoproterozoic	IF	10-15 µm	haematite-quartz		This study
Kittilä jaspers, Finland	ca. 2000 Ma	Jasper	?	haematite		84
Boolgeeda formation, Australia	2400 Ma	BIF (haematite + quartz + magnetite + riebeckite + stilpnomelane + goethite + apatite)	10-15 µm	haematite-quartz	Forms mm thick layers	This study
Hamersley BIF, Dales gorge member, Australia	2500 Ma	BIF (haematite + quartz + magnetite + stilpnomelane + ankerite + minnesotaite + riebeckite)	5-20µm	haematite-quartz		94
				Stilpnomelane and opaque pigments		89
Hamersley BIF, Marra Mamba member, Australia	2500 Ma	BIF (haematite + quartz + magnetite + stilpnomelane + ankerite + minnesotaite + riebeckite)	120-200 nm	haematite-quartz		95
Carajás formation, Brazil	2740 Ma	BIF (haematite + quartz + magnetite)	20-30 µm	haematite-quartz-kerogen		96
Nuvvuagittuq supracrustal belt, Canada	>3770 Ma	BIF (haematite + quartz + magnetite + ripidolite + calcite + chalcopyrite + apatite)	15-30 µm 60-100 µm	haematite-quartz	Small and large varieties. Some have haematite cores and concentric layers	This study

Table S8 Wavelength-dispersive spectroscopy (WDS) analysis of various minerals in the NSB BIF and jaspers.

Mineral (Sample*)	F	Cl	Na_2O	K_2O	MgO	SiO_2	Al_2O_3	CaO	P_2O_5	FeO (Total Fe)	MnO	ZnO	TiO_2	Total
Fluro-apatite (E-F)	1.6	0.1	0.0	0.0	0.0	0.2	0.0	56.2	25.3	0.1	0.0	0.0	0.0	82.9
Fluro-apatite (E-F)	1.4	0.3	0.0	0.0	0.0	0.5	0.0	53.2	26.0	0.2	0.0	0.0	0.0	81.1
Stilpnomelane (E-F)	0.0	0.0	0.0	1.1	4.6	47.9	4.7	0.0	0.0	33.8	0.3	0.0	0.0	92.6
Stilpnomelane (E-F)	0.0	0.0	0.0	1.2	4.5	48.3	4.8	0.0	0.0	34.3	0.3	0.0	0.0	93.4
Magnetite (E-F)	0.0	0.0	0.0	0.0	0.0	0.6	0.1	0.2	0.0	94.3	0.0	0.1	0.0	95.3
Fe-calcite (E-F)	0.0	0.0	0.1	0.0	0.3	0.3	0.3	69.9	0.0	2.8	1.0	0.1	0.0	74.7
Ankerite (D)	0.0	0.0	0.0	0.0	0.4	0.0	0.0	69.6	0.0	4.8	1.6	0.0	0.2	76.4
Mg-ankerite (D)	0.0	0.0	0.0	0.0	16.2	0.2	0.0	30.5	0.0	16.9	1.1	-	-	64.8

*Sample makes reference to thin sections in Figure E3. Low totals attributed to no analysis for REE, hydroxyl and carbon.

Table S9 Raman parameters of graphitic carbon in carbonate rosettes (Fig. E6C).

Grain No.	G-band position	G-band FWHM	D-band position	D-band FWHM	2D-band position	2D-band FWHM	D-band area	G+D2 band area	D/G intensity	2D/ G intensity	T estimate Beyssac[55] ± 50°C
G1	1576	9.78	1339	6.25	N.D	N.D	222.69	749.98	1.32	N.D	539
G2	1567	9.80	1341	9.97	2702	5.41	238.21	803.49	0.32	0.23	539
G3	1565	10.57	1350	6.13	2704	4.71	358.58	640.57	0.41	0.48	481
G4	1579	7.31	1345	11.25	2704	5.54	299.53	369.09	0.56	0.11	441
G5	1557	10.61	1337	9.58	2674	7.94	87.27	355.61	0.13	0.2	553
G6	1569	12.04	1334	15.74	2684	9.22	66.72	158.05	0.61	0.36	509
SG1	1584	5.63	1343	5.77	2708	4.46	140.11	672.22	0.08	0.05	564
SG2	1569	8.98	1331	6.60	2680	5.58	160.64	586.33	0.13	0.12	545
SG3	1577	6.91	1343	12.06	2702	5.66	162.30	500.62	0.18	0.14	532
SG4	1577	6.80	1334	7.68	2696	4.67	167.80	515.40	0.56	0.13	532
SG5	1583	5.65	1347	13.18	2702	5.26	284.12	831.28	0.24	0.05	528
SG6	1569	10.56	1344	6.87	2705	4.95	127.96	367.99	0.44	0.44	526
SG7	1570	10.22	1346	9.73	2725	6.82	122.76	278.79	0.34	0.22	505
SG8	1577	6.29	1345	15.36	2700	5.09	365.76	711.13	0.30	0.16	490
SG9	1565	7.64	1342	7.43	2668	5.21	1203.96	2265.20	0.23	0.08	487
SG10	1580	7.19	1349	7.26	2704	4.58	227.73	371.57	0.28	0.21	472
SG11	1570	8.28	1339	6.63	2705	5.06	604.43	937.62	0.29	0.31	467
SG12	1579	7.32	1345	11.30	2704	5.63	322.68	346.98	0.56	0.12	442
SG13	1583	6.17	1344	12.66	2717	6.58	105.02	119.06	0.37	0.20	432
SG14	1581	10.16	1344	14.20	2676	6.20	657.67	537.29	1.10	0.27	396

* Grains starting with G- are from the Raman scan in Fig 3D and grains starting with SG- are from the Raman scan in Fig E6.

Table S10 Raman parameters of graphitic carbon from NSB jasper sample (Fig. E8E).

G-band position	G-band FWHM	D-band position	D-band FWHM	2D-band position	2D-band FWHM	D-band area	G+D2 band area	D/G intensity	2D/ G intensity	T estimate Beyssac[55] ±50°C
1581	6.18	1359	12.70	2715	9.01	63.77	260.57	0.10	0.24	554
1583	7.29	1348	14.30	2709	10.33	87.76	141.04	0.46	0.51	470
1581	7.03	1346	11.50	2714	12.43	79.70	442.69	0.15	0.25	573

Table S11 Raman parameters of poorly crystalline graphite from NSB. NR – Not resolvable (Fig. E8F).

Spectrum No.	G-band position	G-band FWHM	D-band position	D-band FWHM	2D-band position	2D-band FWHM	D-band area	G+D2 band area	D/G intensity	2D/ G intensity	T estimate Beyssac[55] ± 50°C
1	1585	9.38	1351	8.98	2692	17.55	2614.56	1701.18	1.66	0.45	371
2	1591	7.30	1352	6.15	2701	4.66	1238.30	788.34	2.14	0.14	369
3	1591	7.47	1355	10.10	NR	NR	169.90	87.62	1.91	NR	347